Shallow water bathymetry with multi-spectral satellite ocean color sensors: leveraging temporal variation in image data

Jianwei Wei [1,2*], Menghua Wang [1], Zhongping Lee [3], Henry O. Briceño [4], Xiaolong Yu [5], Lide Jiang [1,6], Rodrigo Garcia [3], Junwei Wang [5], and Kelly Luis [3]

1. NOAA Center for Satellite Applications and Research, College Park, MD 20740, USA
2. Global Science & Technology, Inc., Greenbelt, MD 20770, USA
3. University of Massachusetts Boston, School for the Environment, Boston, MA 02125, USA
4. Florida International University, Southeast Environmental Research Center, Miami, FL 33199, USA
5. Xiamen University, State Key Laboratory of Marine Environmental Science, Xiamen, Fujian 361005, China
6. Colorado State University, Cooperative Institute for Research in the Atmosphere, Fort Collins, CO 80523, USA

Correspondence: jianwei.wei@noaa.gov

Abstract

Polar-orbiting ocean color satellites such as Landsat-8, Suomi National Polar-orbiting Partnership (SNPP), and Sentinel-3 offer valuable image data for the derivation of water bathymetry in optically shallow environments. Because of the multi-spectral limitation, however, it is challenging to derive bathymetry over global shallow waters without reliable mechanistic algorithms. In this contribution, we present and test a physics-based algorithm for improved retrieval of bathymetry with multi-spectral sensors. The algorithm leverages the temporal variation of water-column optical properties in two satellite measurements. By incorporating two remote sensing reflectance spectra in an optimization procedure, it enhances the spectral constraining condition for the optimization, thus leading to improved retrieval accuracy. This scheme was first evaluated using synthetic multi-spectral data. It is shown that the new approach can provide accurate estimation of water depths over 0–30 m range with three types of benthic substrates (corals, seagrass, and sand) and for a wide range of water column optical properties. Based on the degree of improvement, Landsat-8 appears to be benefited the most, followed by SNPP, and then Sentinel-3. The application of the new approach is demonstrated with satellite images over shallow waters (0–30 m) dominated with coral reefs, seagrass, and sand, respectively. This proof-of-concept study confirms the promise of multi-spectral satellite sensors for accurate water depth retrieval by accounting for the temporal characteristics in multiple measurements, suggesting a path forward for the derivation of bathymetry from the existing satellites over global shallow waters.

Keywords: shallow water; bathymetry; spectral optimization; remote sensing reflectance; temporal variation; Landsat-8; SNPP; Sentinel-3.

1. Introduction

Shallow water bathymetry is a basic geophysical parameter of coastal environments. Accurate determination of bathymetry is pivotal for coastal utilization, including navigation, tourism, resource management, and engineering. It is also important for many ecosystem-related studies, such as benthic diversity and class identification, carbon cycling, and water quality. For almost 50 years, the derivation of shallow water bathymetry characteristic of various spatial resolutions has been a hot spot for the ocean remote sensing community.

Advanced methods exist for measuring the bathymetry in shallow environments. Active sensing instruments, such as multi-beam sonar and LiDAR, are widely used for shallow water exploration. Provided necessary support, they allow for accurate bathymetric retrieval over targeted areas (Goodman et al., 2013; McIntyre et al., 2006; Tuell et al., 2005; Wang and Philpot, 2007). Satellite ocean color remote sensing is a passive yet powerful alternative for deriving depth. In optically shallow waters, where the contribution of bottom reflection is non-negligible, the emerging light spectra carry important information on the water depth, bottom albedo, and water column inherent optical properties (IOPs) (Lyzenga, 1978). As such, the remote sensing reflectance ($R_{rs}(\lambda)$) has long been utilized to derive bathymetry maps over optically shallow environments (Brando et al., 2009; Hedley et al., 2016; Klonowski et al., 2007; Kutser et al., 2020; Lee et al., 1999).

There are two main categories of algorithms available for satellite remote sensing of shallow water: empirical approaches and physics-based approaches. The empirical approaches are established upon the statistical relationships between known depth data and $R_{rs}(\lambda)$ measurements at one or several bands (e.g., Stumpf et al., 2003). They are relatively straightforward to implement with either multi-spectral or hyper-spectral satellite images (Caballero and Stumpf, 2019; Liu et al., 2019; McIntyre et al., 2006; Pacheco et al., 2015). In view of the variation of benthic substrates and water IOPs in shallow environments, empirical approaches face hurdles toward global application. Their performance is often dependent on the similarity between data used for algorithm development and those for applications (Dekker et al., 2011). Physics-based or semi-analytical approaches refer to those formulated out of radiative transfer theory (e.g., Lee et al., 1999; Lyzenga et al., 2006; Philpot, 1989). In principle, this type of approach does not need in situ data for model tuning and thus has the potential to be employed for global waters. A caveat is that the shallow water radiative transfer equation is complex to solve, more so than deep waters. According to earlier studies (Lee et al., 1998; Lee et al., 1999), the shallow water properties can be well determined from hyper-spectral $R_{rs}(\lambda)$ data with a spectral optimization algorithm (SOA). The SOA proves to be an effective procedure in estimating the water depth and has been extensively evaluated and continuously refined (Brando et al., 2009; Dekker et al., 2011; Fearns et al., 2011; Giardino et al., 2012; Goodman et al., 2008; Klonowski et al., 2007). The SOA, however, is susceptible to an increase of uncertainty when the band numbers available to the $R_{rs}(\lambda)$ data are significantly reduced, as is the case with multi-spectral sensors (Lee and Carder, 2002; Werdell and Roesler, 2003).

The current polar-orbiting ocean color satellites are generally considered multi-spectral sensors. A non-exhaustive list of multi-spectral satellites includes the fine-spatial resolution (typically less than a few meters) satellites such as WorldView-2 (five visible bands) and RapidEye (three visible bands), the fine-moderate-spatial resolution (~10–30 m) satellites such as Landsat-8 and Sentinel-2 (four visible bands), and the moderate-spatial resolution (~300–1000 m) satellites such as Aqua (seven visible bands) and Sentinel-3 (ten visible bands). The multi-spectral satellite $R_{rs}(\lambda)$ data of different spatial resolutions are increasingly tested for the water depth retrieval in many shallow regions (Caballero and Stumpf, 2019; Cahalane et al., 2019; Li et al., 2019; Stumpf et al., 2003).

Despite the ever-increasing amounts of ocean color images, the small number of bands available to the $R_{rs}(\lambda)$ data has largely limited the applicability of existing physics-based algorithms such as the SOA for shallow water depth retrieval (Barnes et al., 2018; Lee et al., 2010). A gap clearly exists between the need for shallow water bathymetry of fine- to moderate-spatial resolution and the available multi-spectral algorithms useful for the water depth retrieval over global coastal areas.

In this study, we develop and test an optimization approach for improved derivation of bathymetry from multi-spectral ocean color data over global shallow waters. This new approach takes advantage of the temporal variation in the satellite-derived $R_{rs}(\lambda)$ data. The assumption made here is that the temporal variation in two satellite $R_{rs}(\lambda)$ images over a short enough time period is caused by variation in the IOPs, while the bottom albedo (magnitude and shape) and depth remain the same. As such, our optimization algorithm requires two satellite multi-spectral $R_{rs}(\lambda)$ spectra acquired at the same location as input. Distinct from earlier studies, the two $R_{rs}(\lambda)$ spectra are processed simultaneously in the optimization procedure.

Our analysis is focused on three satellite ocean color sensors. With more information given in Table 1, the Landsat-8 Operational Land Imagers (L8/OLI) has four visible bands, including a blue band at 443 nm that was nonexistent on its predecessors (Loveland and Irons, 2016). The Visible Infrared Imaging Radiometer Suite (VIIRS) onboard SNPP has six visible bands, including one aggregated from an imaging band at 638 nm (Wang and Jiang, 2018). The Sentinel-3A Ocean and Land Colour Instrument (S3A/OLCI) has ten visible bands, with a purple band at 400 nm. The model performance is assessed with both synthesized and satellite $R_{rs}(\lambda)$ data. Our results show that the new algorithm can estimate the water depth with improved accuracy, a result of leveraging the temporal variation of the $R_{rs}(\lambda)$ data over the same shallow water pixels.

2. Two-spectrum optimization algorithm

The two-spectrum optimization algorithm, or 2-SOA, works with two multi-spectral remote sensing reflectance spectra, $R_{rs}^{obs}(\lambda, t_1)$ and $R_{rs}^{obs}(\lambda, t_2)$, observed at the same location but at two different times, t_1 and t_2, respectively. The difference between t_1 and t_2 is short enough that the bottom albedo and water depth (after tidal correction) are assumed unchanged. The 2-SOA algorithm first models each of the two reflectances, $R_{rs}^{mod}(\lambda, t_1)$ and $R_{rs}^{mod}(\lambda, t_2)$, as a function of water depth, bottom albedo, and water IOPs. It then evokes spectral optimization to reach an optimal solution for the water depth by searching for the minimum between the two observed and two modeled reflectance spectra. The workflow of the 2-SOA approach for shallow water ocean color inversion of $R_{rs}^{obs}(\lambda, t_1)$ and $R_{rs}^{obs}(\lambda, t_2)$ is illustrated in Figure 1. In the following two subsections, we describe the optical modeling process and spectral optimization, respectively.

2.1 Shallow water optical modeling

We adopt the forward optical models of the hyper-spectral optimization processing exemplar (HOPE) (Lee et al., 1998; Lee et al., 1999) to describe the water-column inherent optical properties and bottom albedo. First, the phytoplankton absorption coefficient ($a_{ph}(\lambda)$) is modeled by an empirical function (Lee et al., 1998)

$$a_{ph}(\lambda) = \left[a_0(\lambda) + a_1(\lambda)\ln a_{ph}(443)\right] a_{ph}(443) \tag{1}$$

where $a_0(\lambda)$ and $a_1(\lambda)$ are wavelength-specific constants initially given from 400 nm to 800 nm for every 10 nm. In this analysis, $a_0(\lambda)$ and $a_1(\lambda)$ are interpolated onto the specific bands of interests. The light absorption of colored dissolved organic matter (CDOM) and detritus (collectively, CDM) are treated together due to the similarity of their spectral behavior, denoted as $a_{dg}(\lambda)$, with

$$a_{dg}(\lambda) = a_{dg}(443)\exp\left[-S_{dg} \times (\lambda - 443)\right] \quad (2)$$

where S_{dg} refers to the spectral slope for $a_{dg}(\lambda)$ in the visible domain and is assumed to be a constant equal to 0.015 nm^{-1}, following Lee et al. (1998). The particle backscattering coefficient ($b_{bp}(\lambda)$) is characterized by a power function,

$$b_{bp}(\lambda) = b_{bp}(443)\left[\frac{443}{\lambda}\right]^{\eta} \quad (3)$$

where the parameter η is estimated from the spectral ratio of $R_{rs}(\lambda)$ at 443 nm and ~550 nm bands, following Lee et al. (2002). Thus, the total absorption and backscattering coefficients can be expressed as

$$a(\lambda) = a_{ph}(\lambda) + a_{dg}(\lambda) + a_{w}(\lambda) \quad (4)$$

$$b_{b}(\lambda) = b_{bp}(\lambda) + b_{bw}(\lambda) \quad (5)$$

where $a_w(\lambda)$ and $b_{bw}(\lambda)$ refer to the absorption and backscattering coefficients of pure seawater, respectively, and are determined as constants following Lee et al. (2015) and Zhang et al. (2009), respectively. The bottom spectrum, $\rho(\lambda)$, is quantified by a normalized bottom albedo spectrum at ~550 nm, $\rho_n(\lambda)$, and a scaling factor, B,

$$\rho(\lambda) = B \cdot \rho_n(\lambda) \quad (6)$$

The $\rho_n(\lambda)$ spectrum is assumed to follow the shape of sandy substrate and adopted from Lee et al. (1999). Figure 2 illustrates the spectral feature for this bottom reflectance spectrum.

With the above-modeled spectral optical properties, the remote sensing reflectance just below the water surface ($r_{rs}(\lambda)$) is approximated following the shallow water model of Lee et al. (1999), as

$$r_{rs}(\lambda) \approx r_{rs}^{dp}(\lambda) \cdot \left\{1 - \exp\left[-\left(\frac{1}{\cos\theta_w} + \frac{D_0\left(1 + D_1 \cdot u(\lambda)\right)^{0.5}}{\cos\theta_a}\right) \cdot k(\lambda) \cdot H\right]\right\} + \frac{\rho(\lambda)}{\pi}\exp\left[-\left(\frac{1}{\cos\theta_w} + \frac{D_0^{'}\left(1 + D_1^{'} \cdot u(\lambda)\right)^{0.5}}{\cos\theta_a}\right) \cdot k(\lambda) \cdot H\right] \tag{7}$$

As shown in Eq. (7), $r_{rs}(\lambda)$ is the sum of the contribution from the water column and the contribution from the bottom reflection. Specifically, $r_{rs}^{dp}(\lambda)$ refers to the reflectance just below the water surface in optically deep waters; the parameter θ_a is the solar-zenith angle and θ_w is the subsurface solar-zenith angle; $k(\lambda)$ is an IOP, with $k(\lambda) = a(\lambda) + b_b(\lambda)$; H is the water depth to be solved; and the values of D_0, D_1, $D_0^{'}$, and $D_1^{'}$ are adopted from Lee et al. (1999),

$$\begin{aligned} D_0 &= 1.03,\ D_1 = 2.4 \\ D_0^{'} &= 1.04,\ D_1^{'} = 5.4 \end{aligned} \tag{8}$$

According to Monte Carlo simulations (Gordon et al., 1988), $r_{rs}^{dp}(\lambda)$ can be estimated by a quadratic function of $u(\lambda)$, as

$$r_{rs}^{dp}(\lambda) = g_0 u(\lambda) + g_1\left[u(\lambda)\right]^2 \tag{9}$$

where $u(\lambda)$ is the ratio of the backscattering to absorption coefficients, with $u(\lambda) = b_b(\lambda)/[a(\lambda) + b_b(\lambda)]$, and two model constants g_0 and g_1 were adopted from Lee et al. (2002), with $g_0 = 0.089$ sr^{-1} and $g_1 = 0.125$ sr^{-1}. We note that the formulation of Eq. (7) provides an explicit description of various contributions to $r_{rs}(\lambda)$ omitting inelastic scattering (Raman scattering and fluorescence) (e.g. Lee and Carder, 2004), which does not make a strong contribution to optically shallow waters.

Lastly, $r_{rs}(\lambda)$ is propagated through the water surface to obtain a $R_{rs}(\lambda)$ spectrum (Lee et al., 1999),

$$R_{rs}(\lambda)=\frac{0.5r_{rs}(\lambda)}{1-1.5r_{rs}(\lambda)} \tag{10}$$

Note that an updated version of Eq. (10) is also available (Lee et al., 2002). The present analysis still uses Eq. (10) to ensure consistency and comparability with earlier studies. Up to this step, each $R_{rs}(\lambda)$ spectrum can be characterized by five unknowns: $a_{ph}(443)$, $a_{dg}(443)$, $b_{bp}(443)$, B and H, i.e.,

$$R_{rs}(\lambda)=\mathrm{Fun}\left[P,G,X,B,H\right] \tag{11}$$

where the parameters P, G, and X refer to $a_{ph}(443)$, $a_{dg}(443)$, and $b_{bp}(443)$, respectively, for simplicity.

2.2 Spectral optimization

The standard HOPE algorithm solves Eq. (11) through a cost function which quantifies the least square residual error (err) between $R_{rs}^{mod}(\lambda)$ and $R_{rs}^{obs}(\lambda)$,

$$err=\frac{\left[\sum\left(R_{rs}^{mod}(\lambda_i)-R_{rs}^{obs}(\lambda_i)\right)^2\right]^{1/2}}{\sum R_{rs}^{obs}(\lambda_i)} \tag{12}$$

Such a cost function is commonly found in ocean color inversions (Dekker et al., 2011; Lee et al., 1999; Roesler and Perry, 1995; Werdell and Roesler, 2003). For convenience, this optimization procedure using one input spectrum will be hereafter called one-spectrum optimization approach, or 1-SOA for short.

The 2-SOA approach considers two independent input spectra obtained at different times. There is no strict requirement for the scale of the time difference. Nevertheless, these two spectra should be measured within a reasonably short period of time, which can be in the order of days or weeks, depending on the availability of utilizable image data. It is important to emphasize that the corresponding bottom albedo and water depth at two observation times should remain (approximately) unchanged, while the water inherent optical properties, including *P*, *G*, and *X* in Eq. (11), can vary. This requirement can be met under most conceivable situations, as abrupt changes of the bottom albedo and water depth are likely caused by extreme events such as hurricanes. The tides can also alter the water levels, which can be corrected (Garcia et al., 2014a). The impact of tidal levels is further discussed later in Section 6.

With two input spectra ($R_{rs}^{obs}(\lambda, t_1)$ and $R_{rs}^{obs}(\lambda, t_2)$), two new remote sensing reflectance spectra can be modeled in the manner analogous to Eq. (11), as

$$\begin{cases} R_{rs}^{mod}(\lambda, t_1) = \mathrm{Fun}\left[P_1, G_1, X_1, B, H\right] \\ R_{rs}^{mod}(\lambda, t_2) = \mathrm{Fun}\left[P_2, G_2, X_2, B, H\right] \end{cases} \tag{13}$$

Note that, in Eq. (13), each modeled reflectance spectrum is characteristic of a unique set of *P*, *G*, and *X* parameters (denoted with subscripts "1" and "2", respectively), but of common bottom albedo and water depth. As a result, Eq. (13) has a total of eight unknowns: P_1, G_1, X_1, P_2, G_2, X_2, *B*, and *H*. To solve Eq. (13) in an optimization procedure, we quantify the difference between the two sets of modeled- and measured-spectra with the cost function given below,

$$err = \frac{\left[\sum\left(R_{rs}^{mod}(\lambda_i, t_1) - R_{rs}^{obs}(\lambda_i, t_1)\right)^2 + \sum\left(R_{rs}^{mod}(\lambda_i, t_2) - R_{rs}^{obs}(\lambda_i, t_2)\right)^2\right]^{1/2}}{\sum R_{rs}^{obs}(\lambda_i, t_1) + \sum R_{rs}^{obs}(\lambda_i, t_2)} \tag{14}$$

We use the MATLAB built-in optimization solver called *fmincon* to search for the minimum for Eq. (14). This routine employs the interior-point algorithm and allows the bound constraints to be applied to each variable. The optimization options include the maximum iterations of 2000 and tolerance of 10^{-5}. The constraints and initial values for the optimization procedure are given in

Table 2. We note that the cost function of Eq. (14) and the standard function of Eq. (12) are essentially the same in the manner that they quantify the minimum. The difference rests on the innovative involvement of two collocated input $R_{rs}(\lambda)$ spectra in the optimization of Eq. (14).

3. Evaluation data

3.1 Synthetic multi-spectral $R_{rs}(\lambda)$ data

The forward models in Eqs. (1)–(10) are used to synthesize a hyper-spectral data set (400–700 nm, for every five nanometers) over shallow waters. The synthetic data mimic real-world optical properties without associated measurement and human errors, and hence provide a straightforward measure to evaluate the algorithm performance (e.g., Barnes et al., 2018; Carder et al., 2005; Garcia et al., 2018; Manessa et al., 2018). The data used here represent a wide range of water depths, IOP combinations, and multiple benthic classes (Table 3). Briefly, the water depths were varied from 0.5 m to 29.5 m with a step of one meter, resulting in 30 depth levels to be assessed. For IOPs, both $a_{ph}(443)$ and $a_{dg}(443)$ were varied from 0.01 to 0.19 m^{-1} with a step of 0.03 m^{-1}. According to analyses of field measurements, the CDM spectral slopes in "clear" waters vary over a relatively narrow range (within ±10% of a median value) across various geomorphic zones (Russell et al., 2019). Therefore, the present study assumed a constant spectral slope with S_{dg} = 0.015 nm^{-1}. Particle backscattering, $b_{bp}(443)$, was varied between 0.001 m^{-1} and 0.019 m^{-1} with an increment of 0.004 m^{-1}. The spectral slope for $b_{bp}(\lambda)$ was varied from –0.5 to 2.5 with a step of 0.5. The solar-zenith angle was assumed to be θ_a = 30°. There are many hyper-spectral bottom spectra measured over various benthic substrates (Hochberg et al., 2003). The inclusion of every spectra in the present simulation would require significant computing capability. Instead, we obtained the median spectra for brown coral, seagrass, and sand from Hochberg et al. (2003) to represent the bottom reflectance spectra for three substrates. As shown in Figure 2, the spectral shape of the sandy substrate is flatter and relatively featureless, while the seagrass spectrum has a broad peak between 500–650 nm and the coral spectrum contains three peaks with a local maximum in the yellow and red domain. Three levels of bottom albedo B were considered for each benthic substrate, with the largest B values assigned to the sandy substrate (Table 3). Finally, for each benthic substrate, a total of 216,090 combinations of water depths (N = 30), bottom albedo (N = 3), and IOPs (N = 2401) were constructed. We acknowledge that realistic benthic spectra are more likely to be mixtures of different species rather than a "pure" type, especially considering the spatial resolution of L8/OLI, SNPP/VIIRS, and S3A/OLCI. Simulation of such mixtures is however beyond the focus of current study.

For each level of simulated water depths and substrates, we randomly chose 400 simulated $R_{rs}(\lambda)$ spectra at each depth level and for each bottom albedo to form the first set of "collocated" spectra, $R_{rs}^{obs}(\lambda, t_1)$. Repeating this process led to the second data set, namely, $R_{rs}^{obs}(\lambda, t_2)$. The resulting collocated $R_{rs}^{obs}(\lambda, t_1)$ and $R_{rs}^{obs}(\lambda, t_2)$ data represent 36,000 pairs of simulations (400 × 30 H × 3 B) with respect to each bottom type. Further, the paired $R_{rs}(\lambda)$ data were spectrally subsampled according to the band settings of L8/OLI, SNPP/VIIRS, and S3A/OLCI. For L8/OLI, we adopted four visible bands of 443, 482, 565, and 665 nm for our analysis. For SNPP/VIIRS, six visible bands of 410, 443, 486, 551, 638, and 671 nm were used. For S3A/OLCI, nine visible bands of 400, 413, 443, 490, 510, 560, 620, 665, and 674 nm were considered. OLCI also has a red band centered at 681 nm, which is omitted in our scheme, given that $R_{rs}(681)$ is subject to the chlorophyll-a fluorescence effect (Gordon, 1979) and the spectral optical models discussed in Section 2.1 do not account for the fluorescence effect.

3.2 Satellite images

We acquired two L8/OLI Level-1 images from the USGS Earth Explorer (Table 1). The observation times for the two images are 16 days apart, which is the revisit period of Landsat-8. According to the NOAA tidal data (https://tidesandcurrents.noaa.gov), both images were captured during the low-tide periods, with the estimated tidal difference within 0.33 meters. The images were processed to Level-2 products with the SeaWiFS Data Analysis System (SeaDAS) (Franz et al., 2015). SeaDAS implements the atmospheric correction developed out of the work of Gordon and Wang (1994). In the analysis, the near-infrared (NIR) and shortwave infrared (SWIR) band combination (865 and 2201 nm) was adopted for the determination of aerosol types, which has been validated for shallow water applications (Wei et al., 2018). An iterative procedure was employed to further correct for the estimated aerosol contributions at the NIR bands (Bailey et al., 2010).

The S3A/OLCI and SNPP/VIIRS images were obtained from the NOAA ocean color data archive (http://coastwatch.noaa.gov) (Table 1). In the Florida Keys, the two Sentinel-3A images were captured around 15:30 UTC, with the estimated tide levels at ~0.3 meters; the tidal difference between the two images is very small. In the Bahamas, the water level differences between two observation times for two collated images were < 0.3 m. We processed the Level-1 images with the Multi-Sensor Level-1 to Level-2 (MSL12) procedure (Wang et al., 2013). MSL12 is based on the NASA SeaDAS 6.4 with modifications and improvements. It can switch among the NIR-, SWIR-, and NIR-SWIR-based atmospheric correction algorithms for open ocean, coastal, and inland waters applications (Wang, 2007; Wang and Shi, 2007; Wang et al., 2009). For SNPP/VIIRS images, a combination of NIR-SWIR bands was used in the current analysis to determine the aerosol types from an aerosol look-up table generated from 12 aerosol models (Wang, 2007). For S3A/OLCI, two NIR bands (779 nm and 865 nm) were chosen for the determination of aerosol types (Gordon and Wang, 1994). The image processing was accomplished with the ocean color data processing system (OCDAPS) at the NOAA Center for Satellite Applications and Research (STAR).

In addition to the above specifics, we kept the default model settings for image processing. The residual glint correction was performed with the standard approach (Wang and Bailey, 2001). The standard Level-2 quality flags, including cloud, high sunglint, straylight, high sensor- and solar-zenith angles, etc., were applied (Mikelsons et al., 2020). Finally, the processed Level-2 images were re-projected onto the Geographic Lat/Lon (WGS 84) Coordinate Reference System (CRS), following the equidistant cylindrical projection. The re-projected images were then collocated using the nearest neighbor resampling procedure.

3.3 Metrics for performance evaluation

To evaluate the algorithm performance in estimating water depth, we calculated the bias ($\bar{\varepsilon}$) as

$$\bar{\varepsilon} = \text{median}\{(M-T)/T\} \times 100\% \tag{15}$$

where M and T refer to the estimated and known values, respectively. Correspondingly, we derived the absolute percentage difference ($|\bar{\varepsilon}|$) as,

$$|\bar{\varepsilon}| = \text{median}\{|(M-T)/T|\} \times 100\% \tag{16}$$

The root-mean-square difference (RMSD) was also computed to assess the model uncertainty, with

$$RMSD = \sqrt{\text{median}\left\{(M - T)^2\right\}} \tag{17}$$

4. Assessment results of the synthetic data

Implementation of the 2-SOA approach with the synthetic data allows insight into the algorithm performance. Along with 2-SOA, we also present the results from the 1-SOA algorithm for which only one $R_{rs}(\lambda)$ spectrum was used. Such comparisons highlight the performance of 2-SOA and the degree of improvement relative to the standard optimization approach.

First, the overall statistical results over the full range of depths (0–30 m) are given in Table 4. It is evident that the 2-SOA approach can estimate water depths with substantially smaller errors ($|\bar{\varepsilon}|$, $\bar{\varepsilon}$, and RMSD) than the 1-SOA approach where one multi-spectral $R_{rs}(\lambda)$ spectrum is used as the input. Among three simulated satellite sensors, L8/OLI has benefited to the largest degree from the 2-SOA approach, mostly because it has the fewest number of wavelengths available for spectral optimization. In contrast, the water depth retrievals for S3A/OLCI have experienced the smallest degree of improvement, because the OLCI has the largest number of bands. The degree of improvement for SNPP/VIIRS remains relatively moderate among three satellites.

Distinctive performance of the 2-SOA algorithm is also revealed in accordance with the benthic substrates, after comparing the statistical results in Table 4. This is expected as 2-SOA assumed a fixed spectrum for the bottom albedo, which is different from the simulated benthic reflectance spectra (recall Figure 2). For the three benthic substrates, the 2-SOA approach yielded the highest degree of improvement for depth retrievals in coral reefs and seagrass environments. The retrievals for sandy environments have also benefited to a relatively smaller extent from the use of two $R_{rs}(\lambda)$ spectra for optimization. This can partially be explained by the very different amplitudes of the bottom albedos. Specifically, sand is usually much brighter and spectrally flatter than coral and seagrass substrates (recall Figure 2 and Table 3) (also see Hochberg et al., 2003). As a result, the subsequent water depth retrievals over sandy substrates tend to be more accurate than the other two bottom types.

We further examined the model performance with respect to its dependence on water depths under investigation. In Figure 3, the absolute percentage errors for the model-estimated depths are plotted as a function of known water depths. For SNPP/VIIRS and S3A/OLCI, the largest errors in retrieved depths are always found in waters where the bottom is shallower than five meters, partially as a result of the small values of water depths themselves. The model errors are generally constrained within ~20% if the waters are deeper than five meters. For L8/OLI, the errors for estimated depths generally increase with the decrease of water depths from about 10 m. For water depths less than three meters, the errors can be in the order of hundreds of percent, particularly over simulated coral and seagrass substrates (Figure 3a and Figure 3d). Besides the small values of water depths themselves, the markedly large errors in waters of less than five meters (Figure 3a, Figure 3d, and Figure 3g) are likely caused by the fact that L8/OLI does not have an additional deep blue band around 412 nm. In waters of 5–30 m, the algorithm appears to perform well with L8/OLI, with acceptably small errors (~20%–30%).

The comparisons in Figure 3 illustrate the performance of the 2-SOA algorithm in improving the water depth retrieval over a wide range of depths. With L8/OLI data, the performance of 2-SOA exceeds 1-SOA at almost every level of depth discussed in this context. The most noticeable improvement for L8/OLI lies in the waters of ~0.5–15 m deep. The degree of improvement, or the absolute difference of the model errors, can be greater than 100% (Figure 3d and Figure 3g). For SNPP/VIIRS and S3A/OLCI, the 2-SOA approach outperforms 1-SOA over the depth range of 5–

20 m. In coral and seagrass substrates, the degree of improvement is about 20% (Figure 3b–Figure 3c, and Figure 3e–Figure 3f); it remains relatively small for sandy bottoms (Figure 3h–Figure 3i).

Since the synthetic data are composed of a wide range of water depths and IOPs, certain combinations of $a(\lambda)$, $b_b(\lambda)$, and H may favor an extremely large water-column attenuating component in Eq. (7), leading to negligible contributions from bottom reflectance. We calculated the ratio of the bottom contribution to the total remote sensing reflectance for each simulation, following $r_{rs}^{b}\% = r_{rs}^{b}(\lambda_{ref})/r_{rs}(\lambda_{ref})\times 100\%$, where $r_{rs}^{b}(\lambda_{ref})$ is the bottom contribution term in Eq. (7) at a reference wavelength (λ_{ref} = 561, 551, and 560 nm for L8/OLI, SNPP/VIIRS, and S3A/OLCI, respectively). In Figure 4, the absolute percentage errors for model-estimated depths are plotted against ten levels of bottom contribution ratios from 0–10% to 90%–100%. As 2-SOA used two synthetic $R_{rs}(\lambda)$ spectra, we chose the maximum $r_{rs}^{b}(\lambda_{ref})$ values as the representative bottom ratio for the two spectra. It can be found that the errors of the derived depths vary with the bottom ratio in a pattern approximately opposite to the model error-depth relationship demonstrated in Figure 3. This is expected and, to a large extent, related to the fact that the bottom reflection tends to contribute more to $R_{rs}(\lambda)$ in shallower environments, in which environments, however, accurate estimation of water depths from 2-SOA (and 1-SOA) is usually more challenging.

5. Assessment results of satellite ocean color images

5.1 Hawaiian coral reefs

The Olowalu Reef (20.79°N–20.81°N, 156.63°W–156.59°W) at the southwest coast of Maui, Hawaii (Figure 5b and Figure 5c) is selected for algorithm evaluation. Located on the leeward side of northeasterly winds and large swells, it represents the largest fringing reef in the main

Hawaiian Islands. This study area covers about three-square kilometers and thus is more suitable for the L8/OLI footprint than the other two sensors. In Figure 6a, the bathymetry map (0–30 m) for this unique reef system is derived from two L8/OLI images using the 2-SOA approach. For comparison, we obtained in situ water depth data from the Scanning Hydrographic Operational Airborne LiDAR survey (SHOALS) (http://www.soest.hawaii.edu/coasts/data/maui/shoals.html). In Figure 6b, the LiDAR data are spatially averaged over pixels within 30 m from the L8/OLI coordinates. First, the satellite- and LiDAR-derived bathymetry maps exhibit almost identical spatial distribution pattern over the range of 0–30 m, which decreases from the coastline towards offshore waters. Figure 6c compares the water depths from L8 and LiDAR in a scatterplot, superimposed with the data density (in colors and contours). Quantitatively, the L8/OLI and LiDAR bathymetry data are consistent with each other except for differences ($|\overline{\varepsilon}|$ = 27%, $\overline{\varepsilon}$ = 21%, RMSD = 5.3 m, and N = 4036). The majority of the data points are distributed closely to the 1:1 line, with a Type-II linear regression equation of Y = 0.96X + 3.21, and R^2 = 0.70. To further validate the L8-derived depths, we extracted the water depth data along the longitudinal lines of 36°37’W, 36°36.5’W, 36°36’W, and 36°35.5’W, respectively. In Figure 7, the similarity of the water depth profiles from L8 and LiDAR is clearly illustrated. Each pair of depth profiles are found with large coefficients of correlation (R^2 = 0.68–0.90), close-to-unity linear regression coefficients, and acceptably small differences ($|\overline{\varepsilon}|$ = 20%–36%, $\overline{\varepsilon}$ = −7.6%–35%, RMSD = 3.1–6.4 m).

The outliers and biases in the L8-generated water depths in Figure 6 and Figure 7 are worth further discussion. In waters of less than five meters, tens of L8-generated depths are found overestimated. These outliers are in part due to the algorithm itself as its performance with four Landsat-8 bands can be somewhat impeded when the water depths are shallow than five meters (e.g., Figure 3). Besides, dozens of L8-derived data points in relatively deep environments (> 10

m) are present around five meters, apparently underestimated in comparison to the LiDAR map. These underestimated data points coincidently aligned themselves with the initial guess for water depth during spectral optimization, suggesting a possible origin. Despite the deviations from the LiDAR data, these outliers only account for a relatively small percentage (< 2%) of the data points, and hence exert limited impact on the consistency between two sets of depth data. It is important to emphasize that the errors of derived depths could be partially due to the complexity of the substrates and uncertainties in the satellite data. The heterogeneous substrates, including the presence of sand channels, independent of coral colonies, or variable morphologies, and the difference in the instruments' footprints, can contribute to the observed uncertainty. In addition, the tide levels (< 0.3 m) at the observation times of L8 images may be partially responsible for the observed positive biases in Figure 6 and Figure 7. Lastly, the disparity between the L8/OLI and LiDAR water depth derivations is, to a certain degree, attributable to the propagation of the uncertainty of the satellite $R_{rs}(\lambda)$ data (e.g., Garcia et al., 2014b; Goodman et al., 2008).

5.2 Florida Keys seagrass environments

The second shallow environment is located in the east of the Florida Keys National Marine Sanctuary (Figure 5d). It covers part of the Florida Bay and the Hawk Channel in the Reef Tract (24.94°N–25.05°N, 80.33°W–80.632°W). This shallow water is characteristic of extensive seagrass beds as well as some typical coral barrier reefs. The study area is large enough (the surface area is about 3.5×6 km^2) to derive and evaluate the water depths from S3A/OLCI images. Note that LiDAR measurements are scarcely available in this region. Instead, the rasterized bathymetry map from the NOAA coastal relief model (CRM) (NGDC, 2001) was acquired for the validation of retrieved water depth from S3A/OLCI. Figure 8a and Figure 8b are the bathymetry maps (0–30

m) derived from S3A/OLCI and CRM, respectively. The S3A- and CRM-derived bathymetry maps are highly comparable to each other. With the majority of the water depths less than ~10 m, the bathymetry in this area gradually increases from the Florida Bay towards the barrier reefs. It also appears that the two bathymetry maps do not sufficiently differentiate land/water pixels in the Florida Bay (northwest to the land shown in Figure 5d), which can be corrected in the future with higher-resolution land masks.

The S3A-derived water depths are quantitatively compared with the CRM data in Figure 8c. To accommodate their different spatial resolutions (~300 m vs. 90 m), the CRM data were averaged over a box of 3×3 pixels centered at the S3A/OLCI coordinates. As the scatterplot shows, two sets of depth data agree with each other very well, with $|\overline{\varepsilon}| = 16\%$, $\overline{\varepsilon} = -3.5\%$, and RMSD = 2.5 m. There exist some data points showing relatively large deviations from the 1:1 line. In the Florida Bay, for instance, a dozen of satellite-derived water depth data are biased high. Two main factors might explain the overestimation in this shallower portion of waters. The first one is related to the possible contamination of S3A/OLCI $R_{rs}(\lambda)$ data; within the S3A/OLCI footprint, narrow sandbars, shoals, and small islands are mixed with surrounding waters, partially impacting the $R_{rs}(\lambda)$ data and subsequent water depth retrievals. Second, it might be a result of the problematic CRM data themselves. After all, the CRM data were generated by spatial interpolation based on many historical low-tide hydrographic data. The instantaneous tide levels are low (< 0.3 m) (Table 1), the impact of which on the comparison is expected to be small. In the relatively deeper waters (> 10 m), the S3A data appear biased low relative to the CRM data. This underestimation is likely related to the bottom heterogeneity around the ~15–30 m isobaths, where the CRM data have undergone spatial gridding, extrapolation, and other arbitrary operations, resulting in possibly unrealistic data.

5.3 The Bahamas

The Bahamas Bank is a massive shallow body of water in the southern Bahamas (22.5°N–25.5°N, 79.5°W–75.75°W) (Figure 5e). The vast shallow area (about 300×300 km^2) is dominated by sandy substrate, with seagrass distributed primarily along the perimeters of the Great Bahamas Bank and the southern bank (Dierssen and Zimmerman, 2003). The extensive flats of the Bahamas are not currently included in the NOAA CRM products. As an alternative, we extracted about 1,200 water depth points from a digital navigation chart – Explorer Charts near the Bahamas, for validation. Figure 9a and Figure 9c show the highly comparable bathymetry maps obtained from the SNPP/VIIRS images and the S3A/OLCI images, respectively. Note that these maps only show the results at pixels for $R_{rs}(443)/R_{rs}(486) < 1$ and $R_{rs}(\sim745) > 0$. Some pixels in the southeastern portion of the shallow area are masked out due to clouds. In the vicinity of Andros Island (24.43°N, 77.95°W), the water depths are largely confined within five meters. Relatively deep waters (around 10 m) are generally found in the middle and southern parts of the bank, similar to the presentation of Lee et al. (2010). In Figure 9b and Figure 9d, the satellite-generated water depths are compared with the depth data extracted from the digital navigation chart. In general, satellite-derived water depths appear to be biased high, with $|\bar{\varepsilon}| = \sim40\%$. This can be largely explained by the fact that the in situ water depth data represent the approximate level of the mean low water springs (MLWS). The satellite-derived depths in our analysis are not corrected for the tide differences either, which are less than half meters at each satellite overpass (Table 1). Dozens of water depths in the northwest edge of the bank are underestimated by satellite data, probably due to the bottom heterogeneity. These underestimated points render the linear regressions deviating to a large degree from the 1:1 line.

Figure 9e is a cross-comparison of the bathymetry data derived from SNPP/VIIRS and S3A/OLCI. The S3A/OLCI depths are averaged over 3×3 pixels to compensate for the difference in two sensors' spatial resolution. As expected, the two sets of water depth estimates are found tightly distributed around the 1:1 line. The differences between two data sets are negligibly small, with $|\bar{\varepsilon}| = 9.3\%$, $\bar{\varepsilon} = -7.3\%$, and RMSD = 1.3 m. We note that the SNPP/VIIRS and S3A/OLCI images were acquired on exactly the same two days, except that the overpass time was slightly different, with SNPP/VIIRS in the early afternoon and S3A/OLCI in the late morning (Table 1). This time discrepancy resulted in different water levels due to the tides, which are, however, negligibly small (and the tide level in this region is usually less than a meter). The consistency between the SNPP/VIIRS and S3A/OLCI depths echoes the assessment results of the synthetic data in Figure 3, where the depths derived with 2-SOA are highly comparable for these two satellites.

6. Discussion

The spectral optimization approach uses typically $R_{rs}(\lambda)$ to estimate multiple shallow water properties including water depth (Dekker et al., 2011; Doerffer and Fisher, 1994; Lee et al., 1998; Lee et al., 1999; Philpot, 1989). This approach is sensitive to the number and position of wavelengths included in $R_{rs}(\lambda)$. In general, a hyper-spectral $R_{rs}(\lambda)$ usually generates much more accurate water depth retrievals than an $R_{rs}(\lambda)$ spectrum with 3–7 bands (Lee and Carder, 2002). The 2-SOA approach takes advantage of the temporal characteristics of water and bottom properties such that it can mitigate the limitation imposed by the few wavelengths to eventually obtain better-constrained retrievals from multi-spectral ocean color observations. Two questions specific to the 2-SOA algorithm are worth further discussion: temporal variation and algorithm limitation.

6.1 Temporal variation of satellite $R_{rs}(\lambda)$

Our analyses demonstrated that 2-SOA could estimate accurate bathymetry by including two reflectance spectra in one optimization procedure (Figure 3 and Table 4). The number of spectra involved in the optimization is the fundamental distinction from the standard approach or 1-SOA. It is also obvious that, if $R_{rs}^{obs}(\lambda, t_1)$ and $R_{rs}^{obs}(\lambda, t_2)$ are the same, the two-spectrum optimization of Eq. (14) will revert to the one-spectrum optimizaiton of Eq. (12). Should such a situation occur, one would expect equivalent performance for 2-SOA and 1-SOA. Thus, it is important to understand that the temporal variation of $R_{rs}(\lambda)$ in shallow environments, specifically, of their absolute spectral values, are caused at least to a large degree by the variation of water IOPs. With the collocated satellite images (Table 1), we assessed the relative percentage difference for satellite-measured $R_{rs}(443)$ values in shallow waters as $\varepsilon = \left[R_{rs}^{obs}(t_1) - R_{rs}^{obs}(t_2) \right] / R_{rs}^{obs}(t_2) \times 100\%$. As shown in Figure 10, the values of $R_{rs}(443)$ in two images are found to vary significantly (far exceeding ±25%) over the vast majority of the shallow waters (0–30 m), supporting the application of 2-SOA. Such temporal variation can be explained by the fact that the shallow waters are liable to the action of wind stress and current advection, and favor a dynamic environment with variable water absorption and backscattering coefficients (Russell et al., 2019).

It is acknowledged that, even with high revisit frequency, two consecutive satellite images will capture image data impacted with different tide phases. In this study, the variation of water level difference due to the tidal influence is usually within half meters, which are small in comparison to the uncertainties of some in situ water depth data. Still, the tide-induced water level difference (ΔH) on two images could result in different $R_{rs}(\lambda)$ spectra. This is expected as the water column contributes to the light attenuation in accordance with the radiance transfer. To understand the role of the tide, we carried out a sensitivity analysis for the $R_{rs}(\lambda)$ spectra based on the model given in Eq. (7). It is assumed that H is the water depth for the first image and $H + \Delta H$ for the second image. We randomly sampled the water IOPs and bottom albedo from the synthetic data for each of the three benthic substrates. As shown in Figure 11, a tide difference between −0.4 m and 0.4 m barely impacts $R_{rs}(443)$ for waters deeper than five meters, irrespective of the bottom types. For waters shallower than five meters, however, ΔH does exert non-negligible influence on $R_{rs}(443)$. The maximum differences are usually present in the shallowest waters; the median absolute percentage errors are less than 20%. Compared with the results given in Figure 10, the influence of the tides on the remote sensing reflectance appears small.

There is limited knowledge of the temporal change of the bottom albedo. A recent satellite analysis reported possible seasonal fluctuations of the bottom albedo (Barnes et al., 2018). This time scale (i.e., seasonal) is long enough that it will not be a problem for obtaining required images from an ocean color satellite. Another study reported rapid wind-driven shifting of unattached benthic macroalgae within half months in the lower Exumas, Bahamas (Dierssen et al., 2009). Furthermore, some benthic substrates and henceforth bottom albedo can also be impacted by extreme weather or long-term climate change (Hoegh-Guldberg, 1999). Such episodic variations in the bottom albedo, if neglected, will cause some errors in water depth retrievals for all algorithms. From an operational perspective, however, these events are less likely to be a ubiquitous matter.

6.2 Limitation and uncertainty

The processing routines of satellite ocean color measurements flag or mask optically shallow pixels (OSP) based on bathymetry. A typical example is the coastal zone (COASTZ) Level-2 quality control flag (l2_flag) developed by NASA. With that flag, the areas shallower than 30 m can be identified as OSP in the ocean color images; a recent update is available from McKinna and Werdell (2018). That approach does not specifically determine whether a pixel is optically shallow, which dictates the range of applicability of the shallow water algorithms including 2-SOA. In the current analysis, we briefly discussed the contribution of bottom reflection to $R_{rs}(\lambda)$ and its potential influence on the algorithm performance. However, it is not clear if a threshold for the bottom ratio can be established to separate optically shallow and deep waters. Such a threshold, if exists, will vary with the bottom types and water's optical properties.

Adoption of a fixed bottom spectrum in the algorithm is common for shallow water remote sensing (Barnes et al., 2018; Goodman et al., 2008; Lee et al., 2010). The reason for this practice lies in the difficulty of determining it from the input $R_{rs}(\lambda)$ spectra. In a recent study, Garcia et al. (2018) demonstrated that the benthic classification based on hyper-spectral $R_{rs}(\lambda)$ data is a very complex problem. The three simulated bottom substrates are specifically intentioned in this study. Despite the uncertainties brought about by the mismatch between them and the bottom spectrum adopted by 2-SOA, our assessments are more realistic than those assuming an exactly known bottom spectrum. Other methods do exist for tackling the bottom spectra, such as the blending of a few pre-fixed bottom spectra (McKinna et al., 2015). A potential problem incurred therein is the addition of at least one new unknown quantity to the optical models/relationships of Eq. (11) and Eq. (13), which might undermine the application of ocean color sensors with too few wavelengths, such as L8/OLI.

The 2-SOA approach estimates bathymetry and other properties simultaneously, including the bottom albedo. After comparing each quantity, we found that the bottom albedo retrievals can also be substantially improved by the 2-SOA approach. In Table 5, the statistical results for estimated bottom albedo at ~555 nm are presented along with those from 1-SOA. The model performance, as demonstrated for B, is very similar to the above observations for water depth retrievals. Yet, the magnitudes of the uncertainties, especially for $|\bar{\varepsilon}|$ and $\bar{\varepsilon}$, are close to 100% even for the 2-SOA approach, partly due to the very small values adopted for B (Table 3). Dependence on water depth is observable for model-derived bottom albedo as well (results not presented). We note that, as the current approach takes a fixed bottom spectrum, it is not clear how to appropriately interpret the resulted bottom albedo.

The spectral optimization approach relies on the accuracy of the absolute values of $R_{rs}(\lambda)$. It is certain that satellite $R_{rs}(\lambda)$ measurements are subject to errors as a result of insufficient calibration and/or atmospheric correction over shallow waters. Recent validation effort has provided preliminary evidence for the $R_{rs}(\lambda)$ errors in shallow waters (Wei et al., 2018). Errors in $R_{rs}(\lambda)$ data can propagate to the subsequent retrieval of water bathymetry (Garcia et al., 2014b). This makes it challenging to compare the satellite-derived bathymetry with field-derived bathymetry. At present, there is a lack of an effective approach to identify the data quality of the satellite $R_{rs}(\lambda)$ spectra in optically shallow environments.

7. Conclusions

Polar-orbiting ocean color satellites image global waters with spectral, spatial and temporal information, providing a great data resource for remote sensing of important shallow water properties. In this study, we presented a novel algorithm that makes use of the temporal variation in satellite $R_{rs}(\lambda)$ data. As the water depth and bottom albedo approximately remain the same at two acquisition times, the temporal variation of $R_{rs}(\lambda)$ is mostly a result of the variation of the water inherent optical properties. As such, our algorithm employs two multi-spectral $R_{rs}(\lambda)$ spectra in one optimization process to obtain better-constrained estimation for water depth. To our knowledge, this study represents the first effort that has considered the temporal variation in the satellite image data for semi-analytical bathymetry retrieval.

We evaluated the two-spectrum optimization algorithm with the synthesized data, with a focus on Landsat-8, SNPP, and Sentinel-3A satellites. The analyses show that the new algorithm can substantially improve the estimation of water depths over coral reef, seagrass, and sand substrates. The most pronounced performance improvement is found with Landsat-8 since it has the smallest number of visible bands. Although the SNPP and Sentinel-3A satellites have different band settings, our analyses show much improved yet comparable water depth retrieval using the new algorithm. This study provides a proof of concept that the temporal variation in multi-spectral satellite ocean color data can be leveraged for accurate water depth retrievals with a physics-based scheme. We acknowledge that there is room for further algorithm improvement. In particular, the retrievals in waters shallower than five meters need to be improved, and more accurate modeling of benthic substrates is still needed. Nevertheless, the new approach has shown to be applicable to Landsat-8, SNPP, and Sentinel-3A and probably many other multi-spectral ocean color satellites for reliable bathymetry derivation.

Acknowledgments

This study was funded by the NOAA Joint Polar Satellite System (JPSS) projects. The NASA Ocean Biology and Biogeochemistry projects (80NSSC18K0509; 80NSSC20K0014; NNX14AQ47A) and Biodiversity and Ecological Forecasting project (NNX15AR96G) provided partial support to the authors (J. Wei; Z. P. Lee). We are grateful to Stuart Phinn and an anonymous reviewer for comments and suggestions. The views, opinions, and findings contained in this paper are those of the authors and should not be construed as an official NOAA or U.S. Government position, policy, or decision.

References

Bailey, S.W., Franz, B.A., & Werdell, P.J. (2010). Estimation of near-infrared water-leaving reflectance for satellite ocean color data processing. *Optics Express, 18*, 7521-7527.

Barnes, B.B., Garcia, R.A., Hu, C., & Lee, Z. (2018). Multi-band spectral matching inversion algorithm to derive water column properties in optically shallow waters: An optimization of parameterization. *Remote Sensing of Environment, 204*, 424-438.

Brando, V.E., Anstee, J.M., Wettle, M., Dekker, A.G., Phinn, S.R., & Roelfsema, C. (2009). A physics based retrieval and quality assessment of bathymetry from suboptimal hyperspectral data. *Remote Sensing of Environment, 113*, 755-770.

Caballero, I., & Stumpf, R.P. (2019). Retrieval of nearshore bathymetry from Sentinel-2A and 2B satellites in South Florida coastal waters. *Estuarine, Coastal and Shelf Science, 226*, 106277.

Cahalane, C., Magee, A., Monteys, X., Casal, G., Hanafin, J., & Harris, P. (2019). A comparison of Landsat 8, RapidEye and Pleiades products for improving empirical predictions of satellite-derived bathymetry. *Remote Sensing of Environment, 233*, 111414.

Carder, K., Cannizzaro, J., & Lee, Z. (2005). Ocean color algorithms in optically shallow waters: limitations and improvements. *Proc. SPIE, 5885*

Dekker, A.G., Phinn, S.R., Anstee, J., Bissett, P., Brando, V.E., Casey, B., et al. (2011). Intercomparison of shallow water bathymetry, hydro-optics, and benthos mapping techniques in Australian and Caribbean coastal environments. *Limnology and Oceanography: Methods, 9*, 396-425.

Dierssen, H.M., & Zimmerman, R.C. (2003). Ocean color remote sensing of seagrass and bathymetry in the Bahamas Banks by high-resolution airborne imagery. *Limnology and Oceanography, 48*, 444-455.

Dierssen, H.M., Zimmerman, R.C., Drake, L.A., & Burdige, D.J. (2009). Potential export of unattached benthic macroalgae to the deep sea through wind-driven Langmuir circulation. *Geophysical Research Letters, 36*, L04602.

Doerffer, R., & Fisher, J. (1994). Concentrations of chlorophyll, suspended matter, and gelbstoff in case II waters derived from satellite coastal zone color scanner data with inverse modeling methods. *Journal of Geophysical Research, 99*, 7475-7466.

Fearns, P.R.C., Klonowski, W., Babcock, R.C., England, P., & Phillips, J. (2011). Shallow water substrate mapping using hyperspectral remote sensing. *Continental Shelf Research, 31*, 1249-1259.

Franz, B.A., Bailey, S.W., Kuring, N., & Werdell, P.J. (2015). Ocean color measurements with the Operational Land Imager on Landsat-8: implementation and evaluation in SeaDAS. *Journal of Applied Remote Sensing, 9*, 096070.

Garcia, R.A., Fearns, P.R.C.S., & McKinna, L.I.W. (2014a). Detecting trend and seasonal changes in bathymetry derived from HICO imagery: A case study of Shark Bay, Western Australia. *Remote Sensing of Environment, 147*, 186-205.

Garcia, R.A., Lee, Z.P., & Hochberg, E.J. (2018). Hyperspectral shallow-water remote sensing with an enhanced benthic classifier. *Remote Sensing, 10*, 147.

Garcia, R.A., McKinna, L.I.W., Hedley, J.D., & Fearns, P.R.C.S. (2014b). Improving the optimization solution for a semi-analytical shallow water inversion model in the presence of spectrally correlated noise. *Limnology and Oceanography: Methods, 12*, 651-669.

Giardino, C., Candiani, G., Bresciani, M., Lee, Z., Gagliano, S., & Pepe, M. (2012). BOMBER: A tool for estimating water quality and bottom properties from remote sensing images. *Computers & Geosciences, 45*, 313-318.

Goodman, J.A., Lee, Z.P., & Ustin, S.L. (2008). Influence of atmospheric and sea-surface corrections on retrieval of bottom depth and reflectance using a semi-analytical model: a case study in Kaneohe Bay, Hawaii. *Applied Optics, 47*, F1-F11.

Goodman, J.A., Purkis, S.J., & Phinn, S.R. (2013). *Coral reef remote sensing-a guide for mapping, monitoring and management*. Dordrecht, Netherlands: Springer, pp. 436.

Gordon, H.R. (1979). Diffuse reflectance of the ocean: the theory of its augmentation by chl a fluorescence at 685nm. *Applied Optics, 18*, 1161-1166.

Gordon, H.R., Brown, O.B., Evans, R.H., Brown, J.W., Smith, R.C., Baker, K.S., & Clark, D.K. (1988). A semianalytic radiance model of ocean color. *Journal of Geophysical Research, 93*, 10909-10924.

Gordon, H.R., & Wang, M. (1994). Retrieval of water-leaving radiance and aerosol optical thickness over the oceans with SeaWiFS: a preliminary algorithm. *Applied Optics, 33*, 443-452.

Hedley, J.D., Roelfsema, C.M., Chollett, I., Harborne, A.R., Heron, S.F., Weeks, S., et al. (2016). Remote sensing of coral reefs for monitoring and management: review. *Remote Sensing, 8*, 118.

Hochberg, E.J., Atkinson, M.J., & Andréfouët, S. (2003). Spectral reflectance of coral reef bottom-types worldwide and implications for coral reef remote sensing. *Remote Sensing of Environment, 85*, 159-173.

Hoegh-Guldberg, O. (1999). Climate change, coral bleaching and the future of the world's coral reefs. *Marine and Freshwater Research, 50*, 839-866.

Klonowski, W.M., Fearns, P.R., & Lynch, M.J. (2007). Retrieving key benthic cover types and bathymetry from hyperspectral imagery. *Journal of Applied Remote Sensing, 1*, 011505.

Kutser, T., Hedley, J., Giardino, C., Roelfsema, C., & Brando, V.E. (2020). Remote sensing of shallow waters – A 50 year retrospective and future directions. *Remote Sensing of Environment, 240*, 111619.

Lee, Z.P., & Carder, K.L. (2002). Effect of spectral band numbers on the retrieval of water column and bottom properties from ocean color data. *Applied Optics, 41*, 2191-2201.

Lee, Z.P., & Carder, K.L. (2004). Hyperspectral Remote Sensing. In R. Miller, C. Del Castillo, & B.A. McKee (Eds.), *Remote sensing of coastal aquatic environment: technologies, techniques and applications* (pp. 181-204). The Netherlands: Springer.

Lee, Z.P., Carder, K.L., & Arnone, R. (2002). Deriving inherent optical properties from water color: a multi-band quasi-analytical algorithm for optically deep waters. *Applied Optics, 41*, 5755-5772.

Lee, Z.P., Carder, K.L., Mobley, C.D., Steward, R.G., & Patch, J.S. (1998). Hyperspectral remote sensing for shallow waters. 1. A semianalytical model. *Applied Optics, 37*, 6329-6338.

Lee, Z.P., Carder, K.L., Mobley, C.D., Steward, R.G., & Patch, J.S. (1999). Hyperspectral remote sensing for shallow waters: 2. Deriving bottom depths and water properties by optimization. *Applied Optics, 38*, 3831-3843.

Lee, Z.P., Hu, C., Casey, B., Shang, S., Dierssen, H., & Arnone, R. (2010). Global shallow-water bathymetry from satellite ocean color data. *EOS, 91*, 429-430.

Lee, Z.P., Wei, J., Voss, K.J., Lewis, M., Bricaud, A., & Huot, Y. (2015). Hyperspectral absorption coefficient of "pure" seawater in the range of 350-550 nm inverted from remote sensing reflectance. *Applied Optics, 54*, 546-558.

Li, J., Knapp, D.E., Schill, S.R., Roelfsema, C., Phinn, S., Silman, M., et al. (2019). Adaptive bathymetry estimation for shallow coastal waters using Planet Dove satellites. *Remote Sensing of Environment, 232*, 111302.

Liu, Y., Deng, R., Qin, Y., Cao, B., Liang, Y., Liu, Y., et al. (2019). Rapid estimation of bathymetry from multispectral imagery without in situ bathymetry data. *Applied Optics, 58*, 7538-7551.

Loveland, T.R., & Irons, J.R. (2016). Landsat 8: the plans, the reality, and the legacy. *Remote Sensing of Environment, 185*, 1-6.

Lyzenga, D.R. (1978). Passive remote-sensing techniques for mapping water depth and bottom features. *Applied Optics, 17*, 379-383.

Lyzenga, D.R., Malinas, N.P., & Tanis, F.J. (2006). Multispectral bathymetry using a simple physically based algorithm. *IEEE Transactions on Geoscience and Remote Sensing, 44*, 2251-2259.

Manessa, M.D.M., Kanno, A., Sagawa, T., Sekine, M., & Nurdin, N. (2018). Simulation-based investigation of the generality of Lyzenga's multispectral bathymetry formula in Case-1 coral reef water. *Estuarine, Coastal and Shelf Science, 200*, 81-90.

McIntyre, M.L., Naar, D.F., Carder, K.L., Donahue, B.T., & Mallinson, D.J. (2006). Coastal bathymetry from hyperspectral remote sensing data: comparisons with high resolution multibeam bathymetry. *Marine Geophysical Researches, 27*, 129-136.

McKinna, L.I.W., Fearns, P.R.C., Weeks, S.J., Werdell, P.J., Reichstetter, M., Franz, B.A., et al. (2015). A semianalytical ocean color inversion algorithm with explicit water column depth and substrate reflectance parameterization. *Journal of Geophysical Research: Oceans, 120*, 1741-1770.

McKinna, L.I.W., & Werdell, P.J. (2018). Approach for identifying optically shallow pixels when processing ocean-color imagery. *Optics Express, 26*, A915-A928.

Mikelsons, K., Wang, M., & Jiang, L. (2020). Statistical evaluation of satellite ocean color data retrievals. *Remote Sensing of Environment, 237*, 111601.

NGDC (2001). *U.S. Coastal Relief Model - Florida and East Gulf of Mexico*. National Geophysical Data Center, NOAA. https://www.ngdc.noaa.gov/thredds/fileServer/crm/crm_vol3.nc.

Pacheco, A., Horta, J., Loureiro, C., & Ferreira, Ó. (2015). Retrieval of nearshore bathymetry from Landsat 8 images: A tool for coastal monitoring in shallow waters. *Remote Sensing of Environment, 159*, 102-116.
Philpot, W.D. (1989). Bathymetric mapping with passive multispectral imagery. *Applied Optics, 28*, 1569-1578.
Roesler, C.S., & Perry, M.J. (1995). In situ phytoplankton absorption, fluorescence emission, and particulate backscattering spectra determined from reflectance. *Journal of Geophysical Research, 100*, 13279-13294.
Russell, B.J., Dierssen, H.M., & Hochberg, E.J. (2019). Water column optical properties of Pacific Coral Reefs across geomorphic zones and in comparison to offshore waters. *Remote Sensing, 11*, 1757.
Stumpf, R.P., Holderied, K., & Sinclair, M. (2003). Determination of water depth with high-resolution satellite imagery over variable bottom types. *Limnology and Oceanography, 48*, 547-556.
Tuell, G., Feygels, V., Kopilevich, Y., Weidemann, A., Cunningham, A.G., Mani, R., et al. (2005). Measurement of ocean water optical properties and seafloor reflectance with scanning hydrographic operational airborne lidar survey (SHOALS): II. Practical results and comparison with independent data. *Proc. SPIE, 5885*
Wang, C., & Philpot, W.D. (2007). Using airborne bathymetric lidar to detect bottom type variation in shallow waters. *Remote Sensing of Environment, 106*, 123-135.
Wang, M. (2007). Remote sensing of the ocean contributions from ultraviolet to near-infrared using the shortwave infrared bands: simulations. *Applied Optics, 46*, 1535-1547.
Wang, M., & Bailey, S. (2001). Correction of the sun glint contamination on the SeaWiFS ocean and atmosphere products. *Applied Optics, 40*, 4790-4798.
Wang, M., & Jiang, L. (2018). VIIRS-derived ocean color product using the imaging bands. *Remote Sensing of Environment, 206*, 275-286.
Wang, M., Liu, X., Tan, L., Jiang, L., Son, S., Shi, W., et al. (2013). Impacts of VIIRS SDR performance on ocean color products. *Journal of Geophysical Research: Atmospheres, 118*, 10,347-310,360.
Wang, M., & Shi, W. (2007). The NIR-SWIR combined atmospheric correction approach for MODIS ocean color data processing. *Optics Express, 15*, 15722-15733.
Wang, M., Son, S., & Shi, W. (2009). Evaluation of MODIS SWIR and NIR-SWIR atmospheric correction algorithm using SeaBASS data. *Remote Sensing of Environment, 113*, 635-644.
Wei, J., Lee, Z.P., Garcia, R.A., Zoffoli, M.L., Armstrong, R., Shang, Z., et al. (2018). An assessment of Landsat-8 atmospheric correction schemes and remote sensing reflectance products in coral reefs and coastal turbid waters. *Remote Sensing of Environment, 215*, 18-32.
Werdell, P.J., & Roesler, C.S. (2003). Remote assessment of benthic substrate composition in shallow waters using multispectral reflectance. *Limnology and Oceanography, 48*, 557–567.
Zhang, X., Hu, L., Twardowski, M.S., & Sullivan, J.M. (2009). Scattering by solutions of major sea salts. *Optics Express, 17*, 19580-19585.

Table 1. Instrument specifications, observation time, data access and processing for three ocean color satellites (Landsat-8, SNPP, and Sentinel-3A). The online NOAA tidal data (https://tidesandcurrents.noaa.gov) were used to estimate the tidal difference for the two collocated satellite images. The tidal data for images of Hawaii, Florida Keys, and the Bahamas shallow waters were specific to the local harbor data of Lahaina (20°53’ N, 156°41’ W), Key Largo (25°17.4’ N, 80°20.3’ W), and North Cat Cay (25°33’ N, 79°17’ W), respectively.

	Landsat-8	**SNPP**	**Sentinel-3A**
Instrument	OLI	VIIRS	OLCI
Spatial resolution (m)	30	750	300
Visible bands (nm)	443, 482, 561, 655	410, 443, 486, 551, 638, 671	400, 413, 443, 490, 510, 560, 620, 665, 674, 681[†]
Data access	USGS	NOAA	NOAA
Processing software	L2GEN	MSL12	MSL12
Atmospheric correction	NIR-SWIR	NIR-SWIR	NIR
Images at t_1 and t_2 (Hawaii)	2017-03-15, 063/048 2017-03-31, 063/048	-	-
Images at t_1 and t_2 (Florida Keys)	-	-	2018-01-13 15:33 UTC 2017-12-29 15:21 UTC
Images at t_1 and t_2 (Bahamas)	-	2019-01-30 18:46 UTC 2019-02-04 18:53 UTC	2019-01-30 15:29 UTC 2019-02-04 14:59 UTC
Tide difference at t_1 and t_2 (m)	< 0.3	< 0.3	< 0.3
Tide levels at t_1 and t_2 (m)	< 0.3	< 0.3	< 0.5

[†] The 681 nm band is excluded from the current analysis

Table 2. Spectral constraints and initial values used by the spectral optimization procedure of the two-spectrum optimization approach (2-SOA). The initial values for *P*, *G*, and *X* are generally adopted from Lee et al. (1999). Note that the wavelengths used for the initial values are specific to the ocean color sensors. When the 550 nm or 670 nm band is not available, an alternative band closest to 550 or 670 nm bands will be used.

	Lower boundary	Upper boundary	Initial values †
P_1 (m^{-1})	0.005	0.35	$0.072\times[R_{rs}^{obs}(443,t_1)/R_{rs}^{obs}(550,t_1)]^{-1.62}$
G_1 (m^{-1})	0.001	0.6	$0.072\times[R_{rs}^{obs}(443,t_1)/R_{rs}^{obs}(550,t_1)]^{-1.62}$
X_1 (m^{-1})	0.0001	0.08	$30\times a_w(670)\times R_{rs}^{obs}(670,t_1)$
P_2 (m^{-1})	0.005	0.35	$0.072\times[R_{rs}^{obs}(443,t_2)/R_{rs}^{obs}(550,t_2)]^{-1.62}$
G_2 (m^{-1})	0.001	0.6	$0.072\times[R_{rs}^{obs}(443,t_2)/R_{rs}^{obs}(550,t_2)]^{-1.62}$
X_2 (m^{-1})	0.0001	0.08	$30\times a_w(670)\times R_{rs}^{obs}(670,t_2)$
B	0.001	0.8	0.5
H (m)	0.1	30.5	5

Table 3. Values of water column inherent optical properties (*P*, *G*, *X*, η, and S_{dg}), water depth (*H*), solar-zenith angle (θ_a), and bottom albedo (*B*) used for modeling the remote sensing reflectance data. Three bottom types (coral, seagrass, and sand) are considered.

Quantities	Values (intervals)	Number of levels
P	0.01–0.19 (0.03)	7
G	0.01–0.19 (0.03)	7
X	0.001–0.019 (0.004)	7
H	0.5–29.5 (1.0)	30
η	−0.5–2.5 (0.5)	7
S_{dg}	0.015	1
θ_a	30°	1
B: coral	0.005, 0.05, 0.1	3
B: seagrass	0.01, 0.035, 0.08	3
B: sand	0.1, 0.25, 0.6	3

Table 4. Retrieval accuracy of water depth (H) derived from the synthetic data with three ocean color satellites (L8/OLI, SNPP/VIIRS, and S3A/OLCI). The results from both the two-spectrum optimization approach (2-SOA) and the standard approach (1-SOA) are provided for comparison of their performance.

		L8/OLI			SNPP/VIIRS			S3A/OLCI		
		coral	seagrass	sand	coral	seagrass	sand	coral	seagrass	sand
1-SOA	$\lvert\bar{\varepsilon}\rvert$	42%	43%	21%	22%	31%	13%	22%	26%	10%
	$\bar{\varepsilon}$	14%	13%	7%	6%	18%	2%	5%	14%	3%
	RMSD ‡	9.3	9.5	6.0	8.8	9.1	4.6	8.3	8.5	4.1
2-SOA	$\lvert\bar{\varepsilon}\rvert$	26%	28%	15%	14%	19%	11%	14%	16%	10%
	$\bar{\varepsilon}$	1%	1%	3%	4%	9%	0%	1%	5%	2%
	RMSD	8.3	8.7	5.2	7.7	8.2	4.0	7.2	7.8	3.9

‡ RMSD is represented in units of meters.

Table 5. Same as Table 4 but for the bottom albedo (B) at a reference wavelength.

		L8/OLI			SNPP/VIIRS			S3A/OLCI		
		coral	seagrass	sand	coral	seagrass	sand	coral	seagrass	sand
1-SOA	$\lvert\bar{\varepsilon}\rvert$	203%	167%	50%	187%	263%	24%	145%	139%	19%
	$\bar{\varepsilon}$	203%	167%	8%	187%	263%	10%	145%	139%	7%
	RMSD ‡	0.18	0.17	0.21	0.21	0.23	0.18	0.19	0.17	0.16
2-SOA	$\lvert\bar{\varepsilon}\rvert$	87%	83%	31%	91%	132%	18%	74%	80%	16%
	$\bar{\varepsilon}$	67%	41%	6%	88%	132%	8%	63%	65%	7%
	RMSD	0.21	0.21	0.21	0.19	0.23	0.17	0.18	0.19	0.16

‡ RMSD is given as dimensionless value.

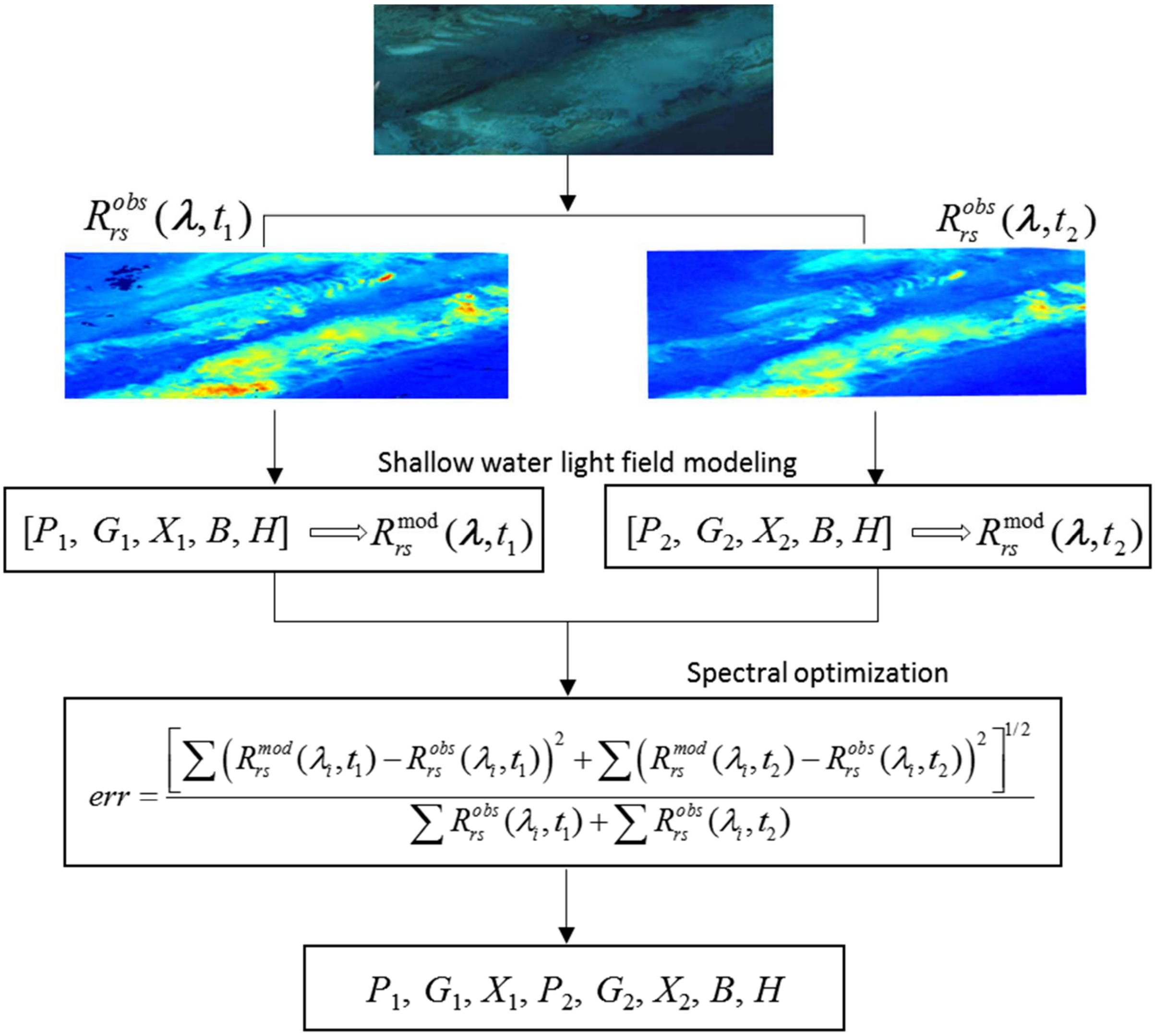

Figure 1. Schematic workflow of the two-spectrum optimization approach (2-SOA) for semi-analytically deriving water depths from two multi-spectral satellite images. Definitions of all quantities: –satellite-observed remote sensing reflectance; –modeled remote sensing reflectance; *P*–phytoplankton absorption coefficient at ~443 nm; *G*–CDM absorption coefficient at ~443 nm; *X*–particle backscattering coefficient at ~443 nm; *B*–normalized bottom albedo at ~550 nm; *H*–water depth; err–least square residual error. The subscripts 1 and 2 refer to the quantities observed, modeled, or derived from two collocated images accessed at observation time t_1 and t_2, respectively.

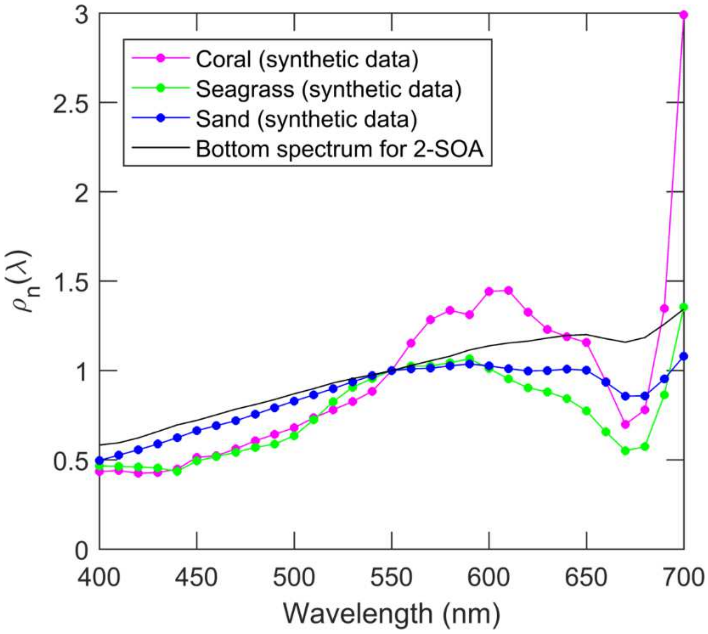

Figure 2. Normalized bottom albedo spectra ($\rho_n(\lambda)$) for coral, seagrass, and sand substrates used for the synthesis of $R_{rs}(\lambda)$ spectra, which were derived from Hochberg et al. (2003). The black curve indicates the bottom albedo spectrum adopted by 2-SOA, which is available from Lee et al. (1999).

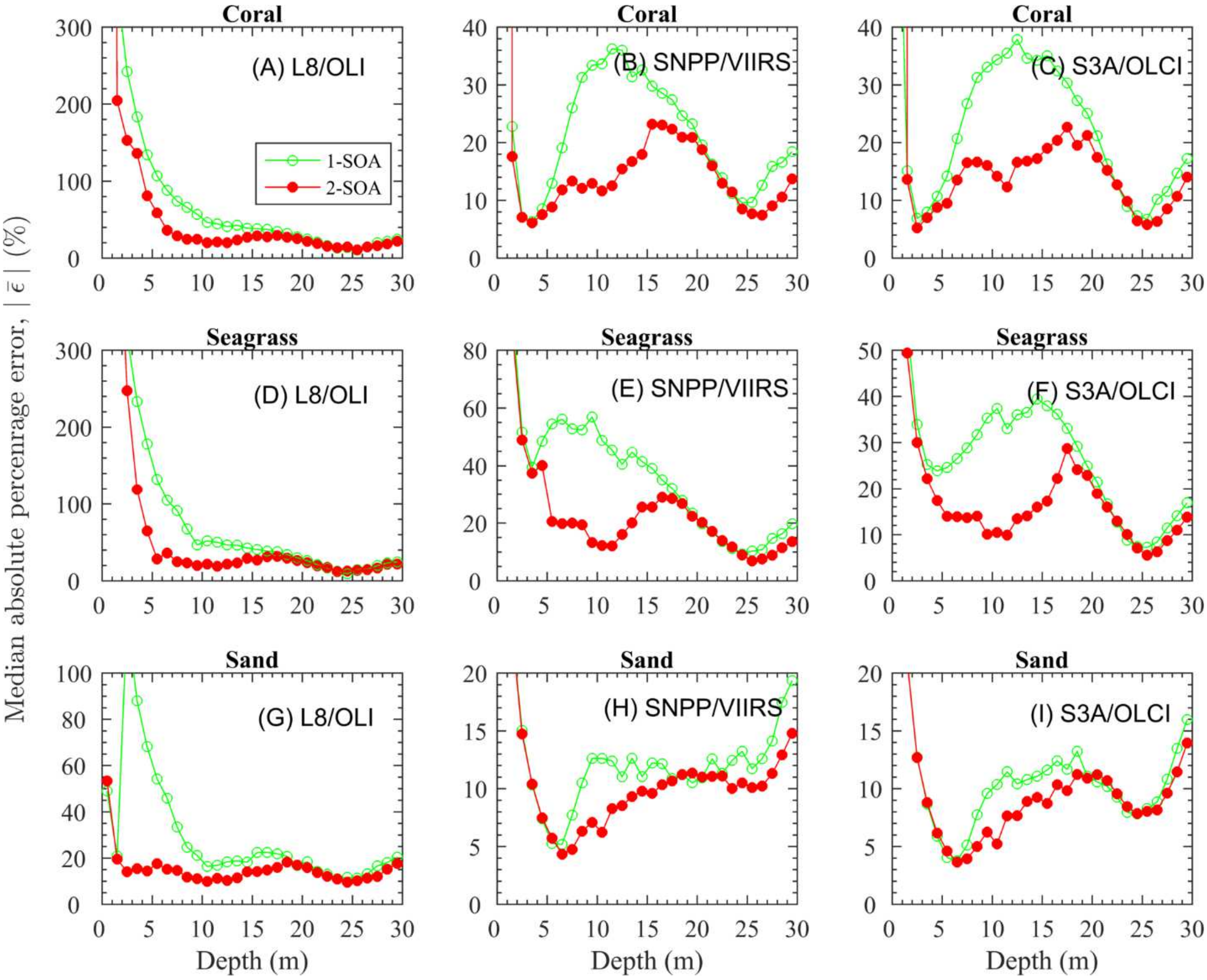

Figure 3. Dependence of the absolute percentage errors ($|\bar{\varepsilon}|$) for the water depth retrieval on the range of known water depths. The two-spectrum optimization approach (2-SOA) and the standard approach (1-SOA) are compared in these illustrations. Each subplot represents a particular bottom type and a specific ocean color sensor combination. Each row indicates the results from different satellites (L8/OLI, SNPP/VIIRS, and S3A/OLCI), while each column refers to the results for different bottom types (coral, seagrass, and sand).

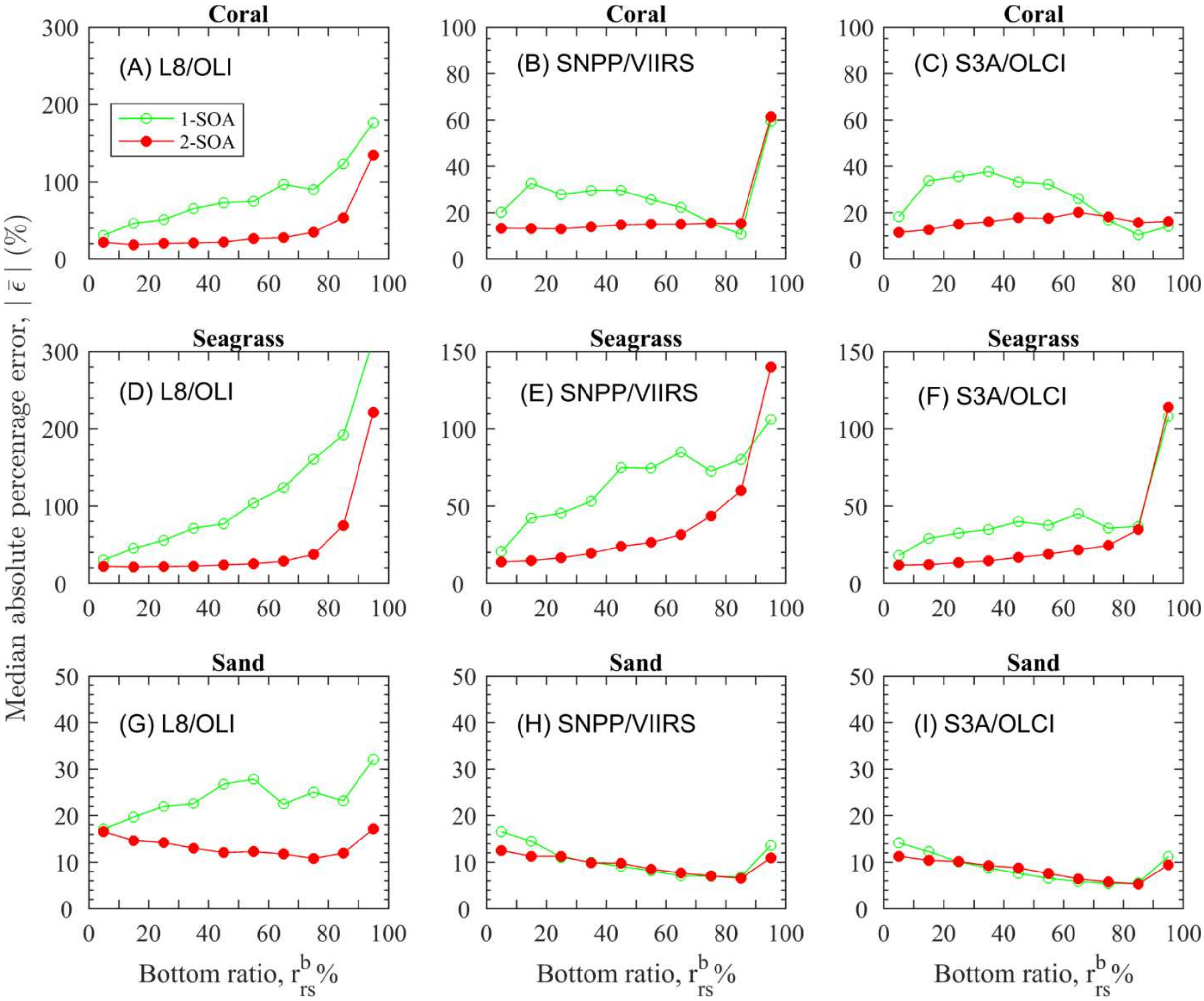

Figure 4. Dependence of the accuracy (specifically, absolute percentage error) of the water depth retrieval on the contribution of bottom reflection. The bottom ratio, or the ratio of bottom reflection contributed to the remote sensing reflectance, is calculated and used as the reference in the x-axis. Each subplot represents a particular bottom type and a specific ocean color sensor combination. Each row indicates the results from different satellites (L8/OLI, SNPP/VIIRS, and S3A/OLCI), while each column refers to the results for different substrates (coral, seagrass, and sand).

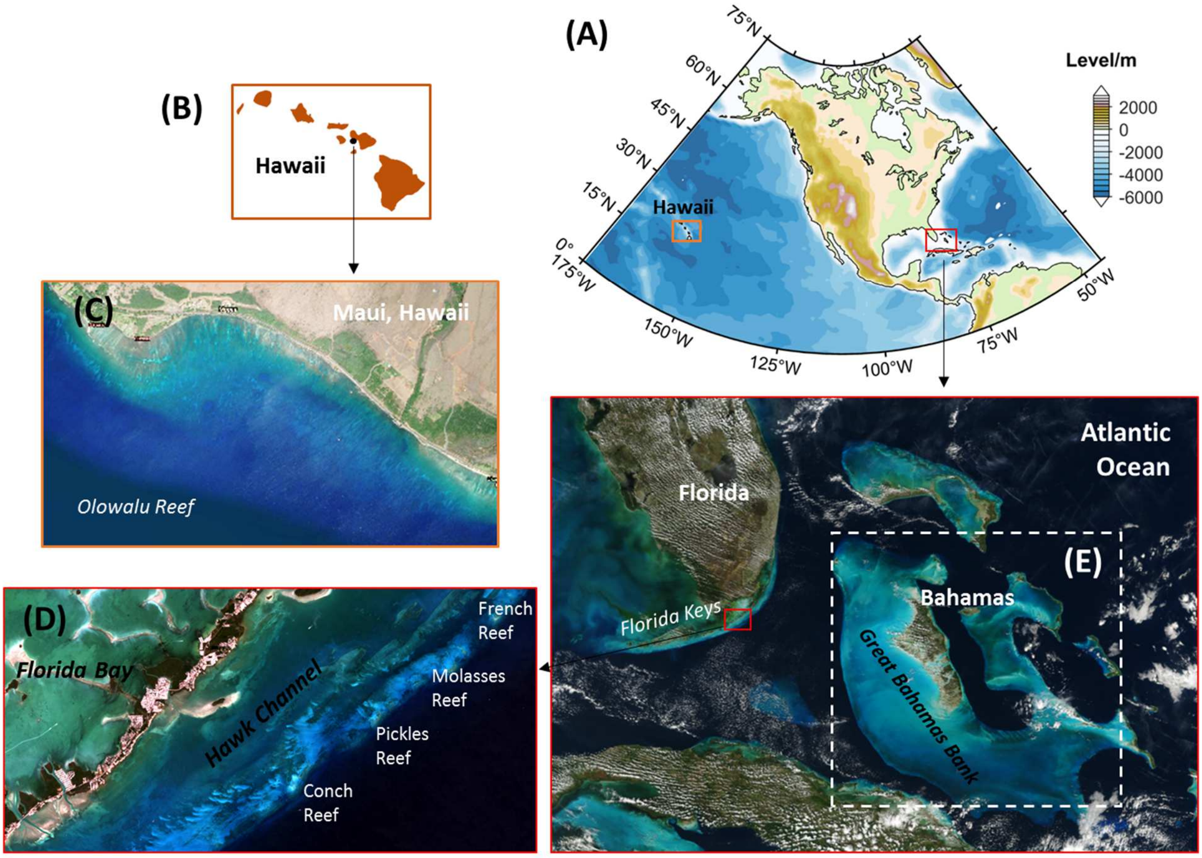

Figure 5. (a) Locations of selected study areas; (b) location of the study area in Hawaii; (c) a true-color image of the coral reefs in Maui, Hawaii; (d) a true-color image of the Florida Keys; and (e) a true-color image of the Bahamas (highlighted in dashed line).

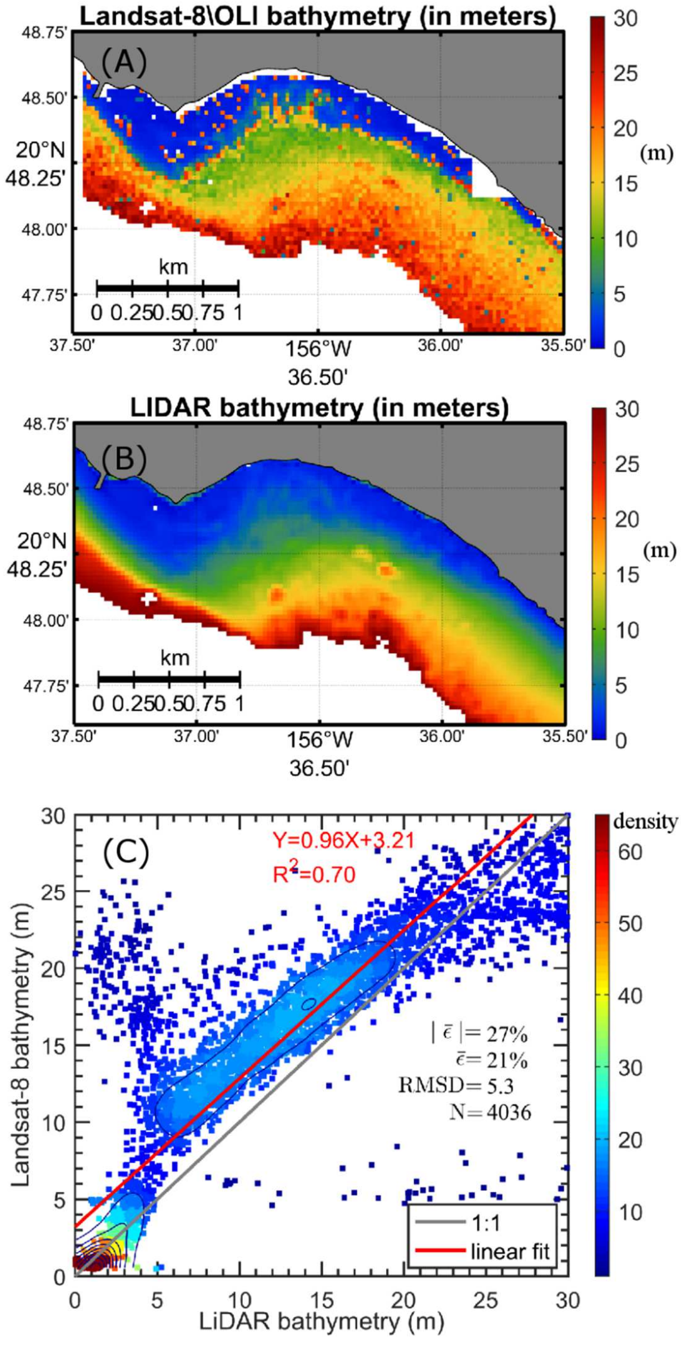

Figure 6. (a) Bathymetry map (in meters) in the reef system of Hawaii derived from the L8/OLI images with the two-spectrum optimization approach (2-SOA). (b) Bathymetry map derived from LiDAR measurements. (c) Scatterplot for the water depths derived from L8/OLI and LiDAR (with colors and contours indicating the data density), where the LiDAR matchup data were determined from the nearest pixels. The red solid line in (c) is the linear regression for L8/OLI- and LiDAR-derived water depths: $Y = 0.96X + 3.21$, $R^2 = 0.70$.

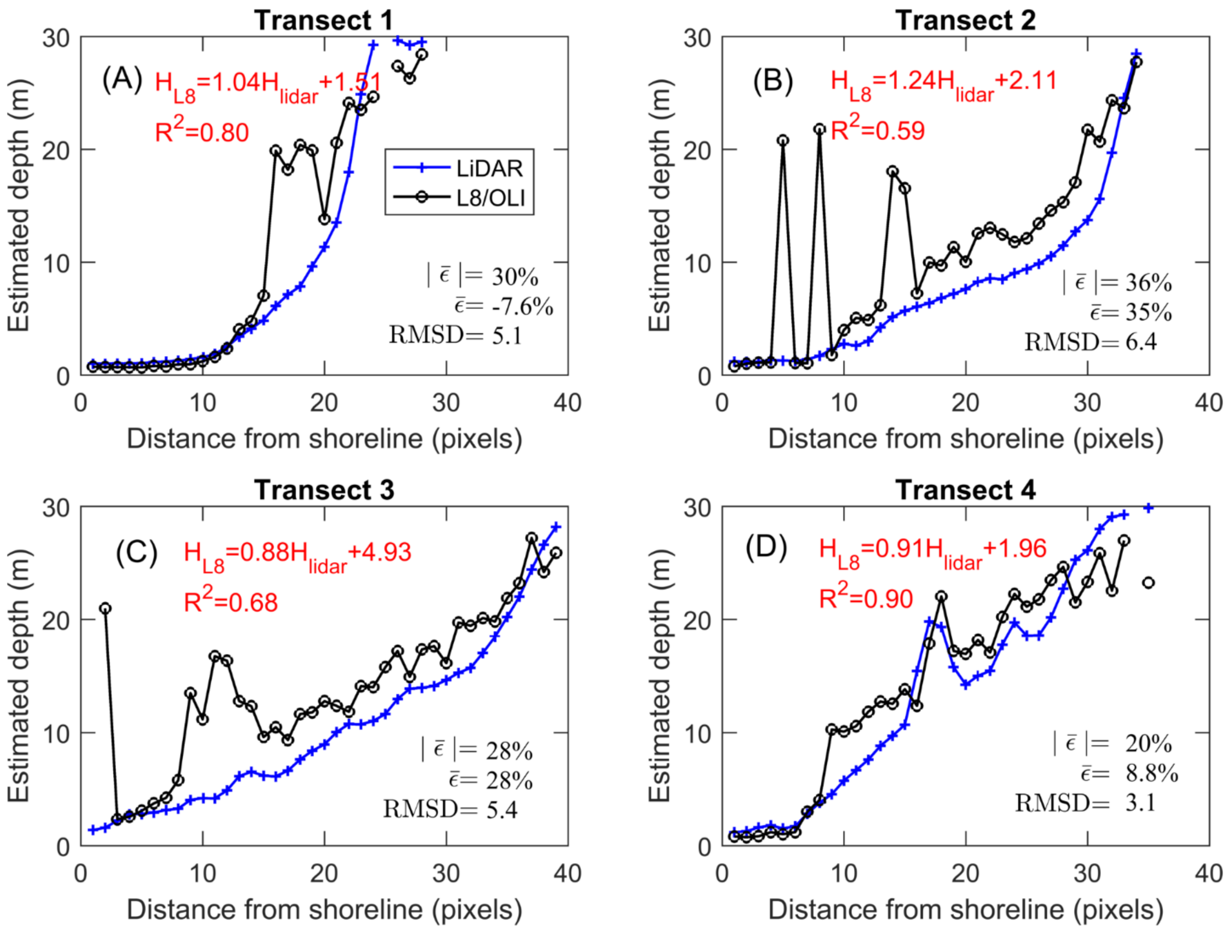

Figure 7. Comparison of the water depth retrievals from the L8/OLI images with the two-spectrum optimization approach (2-SOA) and the LiDAR sensing technique along with four pre-selected meridional transect lines, −36°37’W, −36°36.5’W, −36°36’W, and −36°35.5’W, respectively. The x-axis is given in the number of pixels (40 pixels are equivalent to a horizontal distance of about 1200 m). The equations of the form of $H_{L8} = A \times H_{lidar} + M$ in each subplot refer to the Type-II linear fit between the water depths derived from L8/OLI and LiDAR.

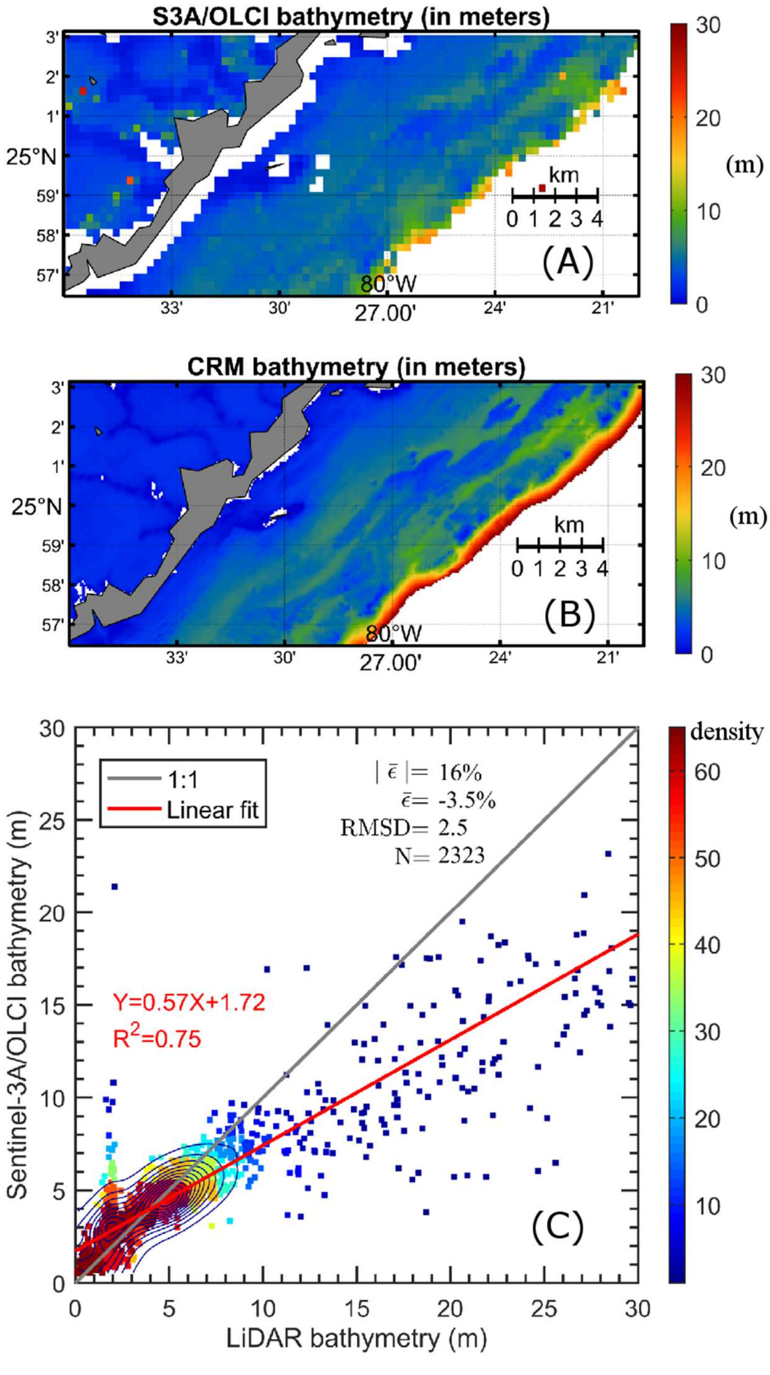

Figure 8. (a) Bathymetry map (in meters) for the seagrass environment of Florida Keys derived from the S3A/OLCI images with the two-spectrum optimization approach. (b) Bathymetry map (in meters) derived from the NOAA CRM model. (c) Scatterplot for the water depth retrievals from S3A/OLCI and CRM (with the colors and contours indicating the data density), where the CRM matchup data were averaged over 3×3 pixels. The red solid line in (c) is the linear regression for L8/OLI- and LiDAR-derived water depths: Y = 0.57X + 1.72, R^2 = 0.75.

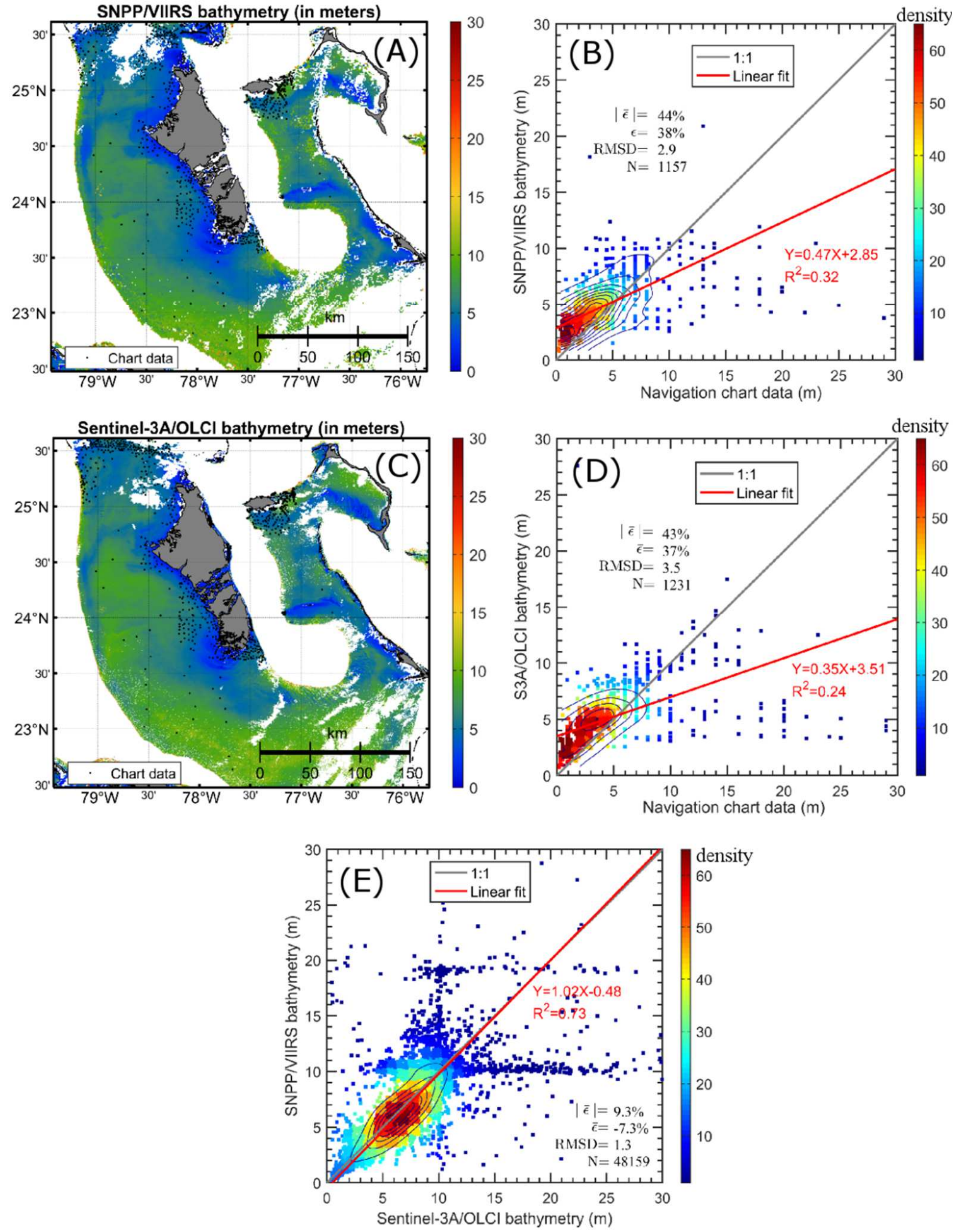

Figure 9. (a) The bathymetric map (in meters) in the Bahamas derived from SNPP/VIIRS images (the black dots indicate the sites with available navigation depth data). (b) Validation of SNPP/VIIRS-derived depths with the water depth data from the nautical chart (with colors and contours indicating the data density). (c) The bathymetry map derived from S3A/OLCI images using 2-SOA (the black dots indicate the sites with available depth data). (d) Validation of S3A-derived depths with the water depth data extracted from the nautical chart. (e) Scatterplot for the water depth retrievals from SNPP/VIIRS and S3A/OLCI; for the latter, the water depths were averaged over 3×3 pixels.

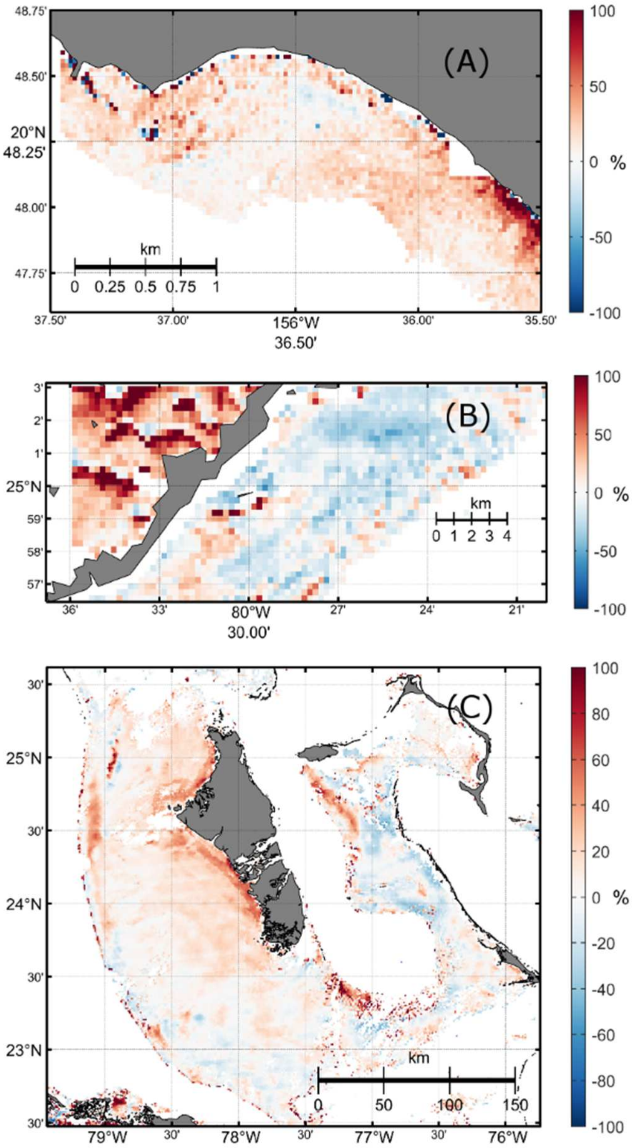

Figure 10. Relative difference (ε) of $R_{rs}(443)$ values in two collocated satellite images in three different benthic environments: (a) coral reefs, (b) seagrass, and (c) sand. The relative difference is derived as $\varepsilon = \left[R_{rs}^{obs}(t_1) - R_{rs}^{obs}(t_2) \right] / R_{rs}^{obs}(t_2) \times 100\%$. The detailed information on the L8/OLI, S3A/OLCI, and SNPP/VIIRS images is given in Table 1.

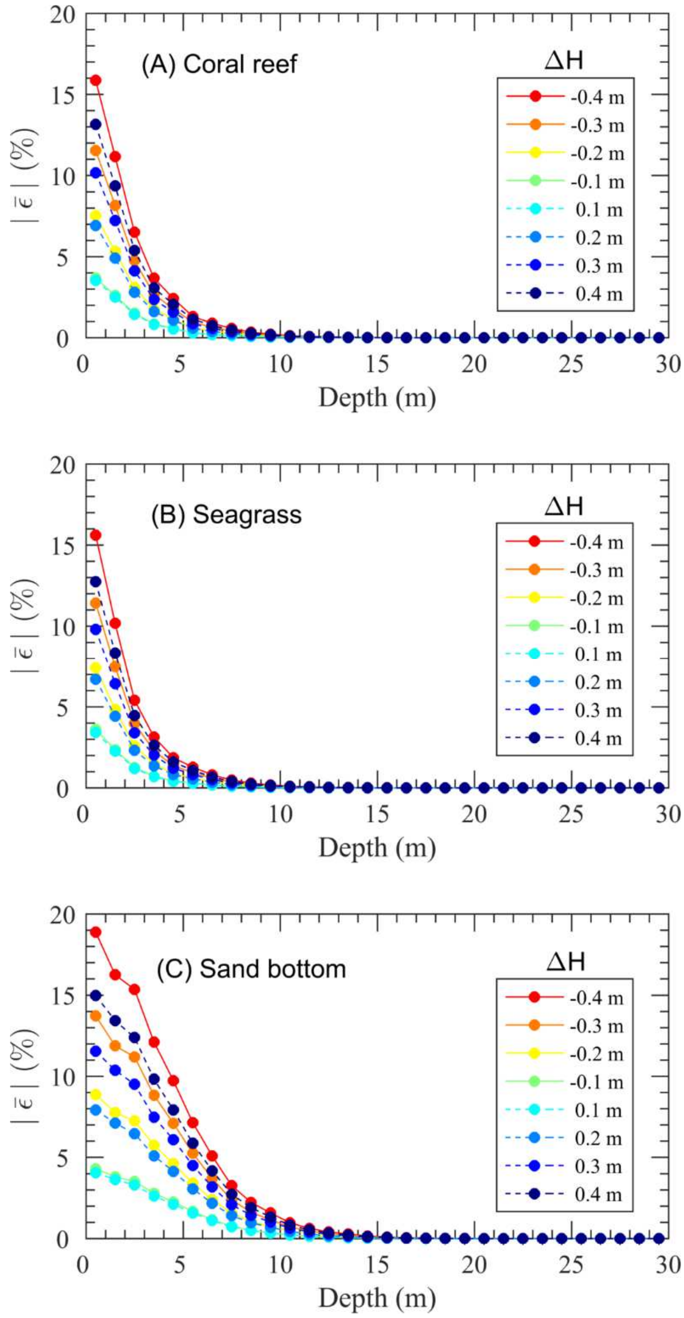

Figure 11. Influence of the water level difference induced by tides (ΔH) on $R_{rs}(443)$ in shallow waters (0–30 m). The simulations considered various inherent optical properties and bottom albedo randomly sampled from the synthetic data for each bottom types; the total number of simulations is 28479. Eight levels of ΔH are considered, which vary from −0.4 m to 0.4 m, with a step of 0.1 m.